Monthly Notices
of the
ROYAL ASTRONOMICAL SOCIETY
MNRAS **485,** 2106–2124 (2019) doi:10.1093/mnras/stz425

Galactic resonance rings: modelling of motions in the wide solar neighbourhood

A. M. Melnik★
Sternberg Astronomical Institute, Lomonosov Moscow State University, Universitetskii pr. 13, Moscow 119991, Russia

Accepted 2019 February 8. Received 2019 February 7; in original form 2018 April 17

ABSTRACT

Models of the Galaxy with analytical Ferrers bars can reproduce the residual velocities of OB associations in the Sagittarius, Perseus and Local System star-gas complexes located within 3 kpc of the solar neighbourhood. Ferrers ellipsoids with a density distribution defined by power indices $n = 1$ and 2 are considered. The successful reproduction of velocity in the Local System is due to the large velocity dispersion, which weakens resonance effects by producing smaller systematic motions. Model galaxies form nuclear, inner and outer resonance rings R_1 and R_2. The outer rings R_2 manage to catch twice as many particles as rings R_1. The outer Lindblad resonance of the bar (OLR) is located 0.4 kpc beyond the solar circle, at $R_{\rm OLR} = R_0 + 0.4$ kpc, corresponding to a bar angular velocity of $\Omega_{\rm b} = 50\,{\rm km\ s^{-1}\ kpc^{-1}}$. The solar position angle with respect to the bar, $\theta_{\rm b}$, that provides agreement between model and observed velocities is 40–52°. Unfortunately, the models considered cannot reproduce the residual velocities in the Carina and Cygnus star-gas complexes. A redistribution of the specific angular momentum, L, is found near the Lindblad resonances of the bar (inner Lindblad resonance (ILR) and OLR): the average value of L increases (decreases) at radii slightly smaller (larger) than those of the resonances, which could be connected with the existence of two types of periodic orbits elongated perpendicular to each other there.

Key words: Galaxy: kinematics and dynamics – open clusters and associations: general – Galaxy: structure.

1 INTRODUCTION

The presence of a bar in the Galaxy is a signpost of the secular evolution of galaxy structure (Kormendy & Kennicutt 2004). After the end of the epoch of violent galaxy–galaxy interactions (~7 Gyr ago), secular processes caused bar formation in disc galaxies. Observations suggest that the fraction of disc galaxies containing a bar decreases towards higher redshifts and that most massive galaxies form bars much earlier than lower mass ones (Sheth et al. 2008; Melvin et al. 2013). Modelling shows that the time-scale over which a bar forms increases strongly with decreasing disc-to-total mass fraction (e.g. Athanassoula & Sellwood 1986; Fujii et al. 2018). Though bars can form spontaneously in dynamically cold discs (Ostriker & Peebles 1973), the bar fraction depends on the environment: in disc-dominated galaxies, tidal interactions can trigger bar formation (e.g. Elmegreen, Elmegreen & Bellin 1990; Mendez-Abreu et al. 2012; Martinez-Valpuesta et al. 2017). Rigid rotation of the bar in a differentially rotating disc causes the appearance of resonances and the formation of resonance rings (Buta 2017).

★ E-mail: anna@sai.msu.ru

There is a lot of evidence that our Galaxy includes a bar. Infrared observations of the inner Galactic plane (Dwek et al. 1995; Benjamin et al. 2005; Cabrera-Lavers et al. 2007; Churchwell et al. 2009; González-Fernández et al. 2012), gas kinematics in the inner Galaxy (Pohl, Englmaier & Bissantz 2008; Gerhard 2011) and an X-shaped distribution of red giants in the central region derived from Bulge Radial Velocity Assay (BRAVA), Wide-Field Infrared Survey Explorer (WISE) and VISTA Variables in the Via Lactea (VVV) data (Li & Shen 2012; Ness & Lang 2016; Simion et al. 2017) confirm the presence of a bar in the Galaxy. Estimates of the length of the bar semi-major axis lie in the range 3–5 kpc, which corresponds to a bar angular velocity of 40–70 km s^{-1} kpc^{-1}.

A resonance between the frequency of orbital rotation with respect to the bar and the frequency of epicyclic motions causes the formation of elliptical resonance rings (Buta 1995; Buta & Combes 1996). The condition for resonance is as follows:

$$\frac{n}{m} = \frac{\kappa}{\Omega - \Omega_{\rm b}}, \tag{1}$$

where n shows the number of full epicyclic revolutions made by a star rotating on a circular orbit around the galactic centre during m orbital revolutions with respect to the bar. Usually the case $m = 1$ is considered. The fraction $n/m = \pm 2/1$ corresponds to the inner (ILR, +2/1) and outer Lindblad resonances (OLR, −2/1); the high-order resonances ±4/1 are also important (Athanassoula 1992; Contopoulos & Grosbol 1989).

Modelling of the resonance rings shows that the outer rings form near the OLR of the bar, while the inner and nuclear rings emerge near the inner 4/1 resonance and the ILR, respectively (Schwarz 1981; Byrd et al. 1994; Rautiainen & Salo 1999, 2000; Rodriguez-Fernandez & Combes 2008; Pettitt et al. 2014; Li, Shen & Kim 2015; Sormani et al. 2018).

The outer rings have two preferable orientations with respect to the bar: rings R_1 are elongated perpendicular to the bar, while rings R_2 are stretched along the bar. Of the two outer rings, R_1 lies somewhat closer to the galactic centre than R_2. Some rings do not have a pure elliptical shape, but include a break so that instead they resemble two tightly wound spiral arms. Broken rings are named pseudorings and are marked with prime symbols, for example, R_1' and R_2' (Buta 1995; Buta & Combes 1996; Buta & Crocker 1991).

All resonance rings are supported by the main periodic orbits. The main periodic orbits are stable orbits, close to circular in the unperturbed case. Such orbits are followed by a large set of quasi-periodic orbits. There are two basic families of stable direct periodic orbits, x_1 and x_2. The family x_2 of stable periodic orbits exists only between two ILRs. There is also a third family of periodic orbits, x_3, which consists of unstable orbits. The main periodic orbits x_1 inside the corotation radius (CR) are elongated along the bar and form the backbone of the bar. The x_2 orbits are elongated perpendicular to the bar and support nuclear rings. Near the OLR of the bar, the main family of periodic orbits x_1 splits into two families: $x_1(1)$ and $x_1(2)$. The main stable periodic orbits $x_1(2)$ lying between the −4/1 and −2/1 (OLR) resonances are elongated perpendicular to the bar, while orbits $x_1(1)$ located outside the OLR are stretched along the bar. Periodic orbits $x_1(2)$ support outer ring R_1, while orbits $x_1(1)$ support outer ring R_2 (Contopoulos & Papayannopoulos 1980; Schwarz 1981; Contopoulos & Grosbol 1989; Buta & Combes 1996).

Studies of invariant manifolds associated with unstable periodic orbits around Lagrangian equilibrium points L_1 and L_2 show that they can also give rise to spiral-like and ring-like structures in barred galaxies (Romero-Gómez et al. 2007; Athanassoula, Romero-Gómez & Masdemont 2009; Jung & Zotos 2016).

Analysis of mid-infrared images of galaxies detected by the *Spitzer* Space Telescope (Sheth et al. 2010) reveals that the fraction of galaxies hosting outer rings or pseudorings increases with increasing bar strength from 15 (SA) to 32 per cent (SA$\underline{\text{B}}$) and then drops to 20 per cent for stronger bars (SB) (Comeron et al. 2014), where the sequence SA, S$\underline{\text{A}}$B, SAB, SA$\underline{\text{B}}$ and SB indicates the increasing contribution of a bar (for example, Buta 2017).

Elmegreen & Elmegreen (1985) discover two types of bar: large bars with nearly constant surface brightness, mostly found in early-type galaxies, and smaller bars with nearly exponential profiles, mainly observed in late-type galaxies. Laurikainen, Salo & Buta (2005) show that 'flat' bars in early-type galaxies can be described well by either a Sérsic or a Ferrers function.

The presence of outer rings in the Galaxy was first suggested by Kalnajs (1991). The main advantage of models with outer rings is that they do not need a spiral-like potential perturbation to create long-lived elliptical structures at the galactic periphery. Outer rings form within 200–500 Myr after bar formation and can exist for several Gyr (Rautiainen & Salo 2000; Rautiainen & Melnik 2010).

The angle between the major axis of the bar and the Sun–Galactic Centre line or the so-called solar position angle with respect to the bar, θ_b, derived from data of infrared surveys (Galactic Legacy Infrared Mid-Plane Survey Extraordinaire (GLIMPSE), Two-Micron All-Sky Survey (2MASS) and VVV), has a value of 40–45°, so that the end of the bar closest to the Sun is located in the first quadrant (Benjamin et al. 2005; Cabrera-Lavers et al. 2007; González-Fernández et al. 2012). Additionally, a reconstruction of Galactic CO maps with smoothed particle hydrodynamics gives the best results for a solar position angle of $\theta_b \approx 45°$ (Pettitt et al. 2014).

Melnik & Rautiainen (2009), using models with analytical Ferrers bars, study the Galactic kinematics in the 3-kpc solar neighbourhood. Their models form two-component outer rings R_1R_2' after ∼800 Myr from the start of the simulation. The gas subsystem includes 5×10^4 massless gas particles, which can collide with each other inelastically. The best agreement between model and observed velocities corresponds to solar position angle $\theta_b = 45 \pm 5°$. These models can reproduce the average velocities of OB associations in the Perseus and Sagittarius star-gas complexes, but fail in the Local System, Cygnus and Carina star-gas complexes.

The fact that the position angle of the Sun with respect to the bar, θ_b, is close to 45° means that a 3-kpc solar neighbour can harbour both a segment of the outer ring R_1 and a segment of ring R_2. The study of the distribution of classical Cepheids and young open clusters reveals the existence of a 'tuning-fork-like' structure, which can be interpreted as two segments of the outer rings fusing together near the Carina star-gas complex (Melnik et al. 2015, 2016). Note also that models with a two-component outer ring R_1R_2' can explain the position of the Sagittarius–Carina arm in the Galactic disc: a segment of the ring R_1 outlines the Sagittarius arm, while an arch of the outer ring R_2 lies in the vicinity of the Carina arm (Melnik & Rautiainen 2011).

Rautiainen & Melnik (2010) build *N*-body models of the Galaxy, which demonstrate the development of a bar and the formation of the outer rings, which, once formed, persist till the end of the simulation (6 Gyr). A special feature of *N*-body models is fast changes of velocities of model particles, which can be separated into quick stochastic changes due to irregular forces and quasi-periodic slow oscillations due to slow modes (patterns rotating more slowly than the bar). Thus, the averaging of model velocities over a large time interval is required for a comparison with observed velocities. In the *N*-body models by Rautiainen & Melnik (2010), the velocities of model particles are averaged over a time interval of 1 Gyr in a reference system corotating with the bar. The averaged model velocities appear to be able to reproduce the observed velocities in the Sagittarius, Perseus and Local System star-gas complexes. The advantage of models without self-gravity in kinematical studies is that they enable us to compare observe and model velocities directly without averaging.

Models presented here do not include spiral arms, because both resonance rings and spiral arms are invoked to explain the same things: systematic velocity deviations from the rotation curve and the increased density of young objects in some regions. Any travelling spiral density wave (Lin & Shu 1964) winds up around the Lindblad resonances after a few time revolution periods (Toomre 1969). The mechanism *Wave Amplification via Stimulated Emission of Radiation* (WASER) including the reflection of the travelling wave in the central region can support a steady spiral pattern (Mark 1976; Bertin & Lin 1996), but it gives a small amplification to support shock fronts as well (Athanassoula 1984; Binney & Tremaine 1987). The shock fronts forming in spiral arms due to collisions in the gas subsystem act in the same direction, causing the drift of gas from the CR towards the Lindblad resonances (Toomre 1977). Another conception of galactic spiral structure suggests short transient spiral arms forming in self-gravitating galactic discs due to a swing amplification mechanism (Julian & Toomre 1966; Toomre 1981). This mechanism can be very powerful and transient ragged spiral arms often appear in simulations with live discs (Baba et al. 2009; Grand, Kawata & Cropper 2012; Baba, Saitoh & Wada 2013; D'Onghia, Vogelsberger & Hernquist 2013; Pettitt et al. 2015 and other articles). However, the pitch angle of these short-lived arms is quite large, $i = 20$–$30°$. The theoretical prediction of its value is $i = 24°$ (Melnik & Rautiainen 2013; Michikoshi & Kokubo 2014), but the Galactic global spiral arms seem to have a considerably smaller pitch angle, 10–15° (for example, Georgelin & Georgelin 1976; Russeil 2003; Vallée 2015, and references therein). Generally, the conception of the Galactic spiral arms has a lot of difficulties. Nevertheless, many kinematical and morphological features of the Galaxy can be explained in terms of spiral arms (Rastorguev et al. 2017; Antoja et al. 2018; Bobylev & Bajkova 2018; Grosbøl & Carraro 2018; Kawata et al. 2018; Ramos, Antoja & Figueras 2018; Xu et al. 2018 and other articles).

In this article, I present several models with analytical Ferrers bars, which can reproduce the observed velocities in the Sagittarius, Perseus and Local System star-gas complexes. The crucial factor that determines success in the Local System appears to be a large velocity dispersion, which weakens resonance effects. Section 2 considers the distribution of observed velocities of young stars in the Galactic disc; Section 3 describes the models; Section 4 compares model and observed velocities and studies the distribution of surface density, velocity dispersion and angular momentum along the radius; Section 5 infers the main conclusions.

2 THE OBSERVED VELOCITIES OF OB ASSOCIATIONS IN THE 3-KPC SOLAR NEIGHBOURHOOD

The velocities of OB associations give the most reliable information about the distribution of velocities of young objects in a wide solar neighbourhood. The catalogue by Blaha & Humphreys (1989) includes 91 OB associations, ∼85 per cent of which include at least one star of spectral type earlier than B0, the age of which is supposed to be less than 10 Myr (Bressan et al. 2012), so the average velocities of OB associations must be very close to the velocities of their parent giant molecular clouds. Here we consider velocities obtained with *Gaia* DR2 proper motions (Brown et al. 2018; Lindegren et al. 2018; Katz et al. 2018). Note that the sky-on velocities of OB associations derived from *Gaia* DR1 and *Gaia* DR2 proper motions differ on average by 2 km s^{-1} (for more details, see Melnik & Dambis 2017).

For comparison with models, we use the residual velocities of OB associations, which characterize non-circular motions in the Galactic disc. The residual velocities are determined as differences between the observed heliocentric velocities and the velocities due to the Galactic circular rotation curve and solar motion towards the apex ($V_{\rm res} = V_{\rm obs} - V_{\rm rot} - V_{\rm ap}$). The radial and azimuthal components, $V_{\rm R}$ and $V_{\rm T}$, of the residual velocity are positive if they are directed away from the Galactic Centre and in the sense of Galactic rotation, respectively. The residual velocity along the z-axis, V_z, is positive in the direction toward the North Galactic Pole. The parameters of the rotation curve and solar motion are derived from the entire sample of OB associations with known line-of-sight velocities and *Gaia* DR2 proper motions (Melnik & Dambis 2017, in preparation). Residual velocities determined with respect to a self-consistent rotation curve are practically independent of the choice of value of the Galactocentric distance of the Sun, R_0.

Fig. 1 shows the residual velocities of OB associations in the Galactic plane. To mitigate random errors, we average the residual

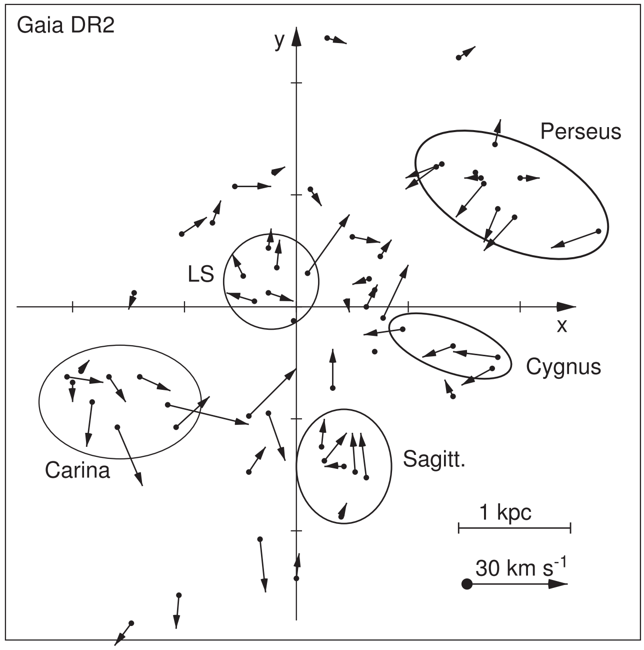

Figure 1. Distribution of the residual velocities of OB associations in the Galactic plane. The residual velocities are derived with the use of *Gaia* DR2 proper motions. OB associations with residual velocities $|V_{\rm R}|$ and $|V_{\rm T}|$ smaller than 3 km s^{-1} are shown as black circles without any vector. The ellipses indicate the positions of the Sagittarius, Carina, Cygnus, Local System (LS) and Perseus star-gas complexes. The x- and y-axes are directed towards the Galactic rotation and away from the Galactic Centre, respectively. The Sun is at the origin.

velocities of OB associations within the volumes of the star-gas complexes identified by Efremov & Sitnik (1988). Table 1 gives the name of the star-gas complex, its Galactocentric distance R, the list of OB associations related to it, the range of their Galactic longitudes l and heliocentric distances r, and their average residual velocities: $V_{\rm R}$, $V_{\rm T}$ and V_z. OB associations having at least two stars with known line-of-sight velocities and *Gaia* DR2 proper motions are considered.

The Galactocentric distance of the Sun is adopted as $R_0 = 7.5$ kpc (Glushkova et al. 1998; Nikiforov 2004; Feast et al. 2008; Groenewegen, Udalski & Bono 2008; Reid et al. 2009; Dambis et al. 2013; Francis & Anderson 2014; Boehle et al. 2016; Branham 2017). A choice of R_0 in the range 7–9 kpc has small influence on the residual velocities.

Fig. 1 and Table 1 indicate that the majority of OB associations in the Perseus complex have the radial component of the residual velocity, $V_{\rm R}$, directed toward the Galactic Centre, while the velocities $V_{\rm R}$ of most OB associations in the Sagittarius and Local System complexes are directed away from the Galactic Centre. As for the azimuthal residual velocities, the majority of OB associations in the Perseus complex have $V_{\rm T}$ directed in a sense opposite to that of Galactic rotation, while $V_{\rm T}$ is close to zero in the Sagittarius and Local System complexes. Only the residual velocities in the Sagittarius, Perseus and Local System star-gas complexes can be reproduced in the present dynamical models. The residual velocities in the Cygnus and Carina complexes still remain a stumbling block for numerical simulations as far as both types of model are concerned: analytical bars and N-body simulations (Melnik & Rautiainen 2009; Rautiainen & Melnik 2010).

Table 1. The observed residual velocities of OB associations in star-gas complexes with *Gaia* DR2 data.

Complex	R kpc	V_R km s^{-1}	V_T km s^{-1}	V_z km s^{-1}	l deg.	r kpc	Associations
Sagittarius	6.0	$+7.5 \pm 2.1$	-0.3 ± 1.7	-0.6 ± 1.8	8–23°	1.3–1.9	Sgr OB1, OB4, OB7, Ser OB1, OB2, Sct OB3
Carina	6.9	-6.2 ± 2.6	$+6.2 \pm 2.8$	-1.9 ± 0.7	286–315°	1.5–2.1	Car OB1, OB2, Cru OB1, Cen OB1
							Coll 228, Tr 16, Hogg 16, NGC 3766, 5606
Cygnus	7.3	-4.3 ± 1.3	-10.3 ± 1.4	$+2.0 \pm 1.4$	73–78°	1.0–1.8	Cyg OB1, OB3, OB8, OB9
Local System	7.8	$+5.4 \pm 2.6$	$+1.2 \pm 2.6$	-0.1 ± 0.5	0–360°	0.3–0.6	Per OB2, Ori OB1, Mon OB1, Vela OB2
							Coll 121, 140
Perseus	8.8	-4.7 ± 2.2	-4.4 ± 1.7	$+0.5 \pm 0.6$	104–135°	1.8–2.8	Cep OB1, Per OB1, Cas OB1, OB2, OB4
							OB5, OB6, OB7, OB8, NGC 457

Table 2. General parameters of model 1.

Simulation time	$T = 2$ Gyr
Step of integration	$\Delta t = 0.01$ Myr
Number of particles	$N = 10^5$
Bulge	$R_{bg} = 0.30$ kpc $M_{bg} = 5\times10^9\,\mathrm{M}_\odot$
Bar	$a = 4.2$ and $b = 1.35$ kpc $M_b = 1.30\times10^{10}\mathrm{M}_\odot$ $\Omega_b = 50.0\,\mathrm{km\,s^{-1}\,kpc^{-1}}$ $T_{gr} = 492$ Myr
Disc	exponential, $R_d = 2.5$ $M_d = 3.5\times10^{10}\,\mathrm{M}_\odot$
Halo	$R_h = 8$ kpc $V_{max} = 206\,\mathrm{km\,s^{-1}}$
Collisions	absolutely inelastic $\varepsilon = 0.05$ pc
OB particles	$t_{ob} = 4$ Myr – lifetime $P_c = 0.1$ – probability
Initial distribution	uniform within $R < 11$ kpc $\sigma_0 = 5\,\mathrm{km\,s^{-1}}$

Table 1 also shows that the average velocities in the z-direction, V_z, are close to zero. Here we suppose that motions in the Galactic plane and in the z-direction are independent, which allows us to use 2D models.

Note that the models considered must also reproduce the Galactic rotation curve determined for the sample of OB associations. To avoid systematic effects, we must use the same sample of objects for the study of residual velocities and determination of the parameters of the rotation curve. The rotation curve derived from the velocities of OB associations is nearly flat and corresponds to the angular velocity at a solar distance of $\Omega_0 = 31 \pm 1\,\mathrm{km\,s^{-1}\,kpc^{-1}}$ (Melnik & Dambis 2017, in preparation).

3 MODELS

I have built several models with analytical Ferrers bars (Ferrers 1877), which can reproduce the kinematics in the Perseus, Sagittarius and Local System star-gas complexes. Some of them are discussed here.

Table 2 lists the general parameters of model 1: the time of simulation T, time step of integration Δt and number of particles N. We neglect the self-gravity between model particles. The massless test particles can be thought as low-mass gas clouds moving in the potential created by the stellar subsystem. The orbits of model particles are calculated with the use of the leapfrog method.

All models include a bar, a disc, a bulge and halo, the parameters of which are given in Table 2. The bar is modelled as a Ferrers ellipsoid with volume-density distribution ρ defined as follows:

$$\rho = \begin{cases} \rho_0(1-\mu^2)^n, & \mu \le 1, \\ 0, & \mu > 1, \end{cases} \tag{2}$$

where μ equals $\mu^2 = x^2/a^2 + (y^2 + z^2)/b^2$, but a and b are the lengths of the major and minor semi-axes of the bar, respectively. Here we consider 2D models, so $z = 0$. The acceleration created by the bar depends on the mass of the bar M_b, semi-axes a and b, the coordinates (x, y) reckoned with respect to the bar axes and the power index n (de Vaucouleurs & Freeman 1972; Pfenniger 1984; Binney & Tremaine 1987; Sellwood & Wilkinson 1993).

The angular velocity of the bar, Ω_b, that provides the best agreement with observations appears to be $\Omega_b = 50\,\mathrm{km\,s^{-1}\,kpc^{-1}}$. Non-axisymmetric perturbations of the bar grow slowly, approaching full strength at $T_{gr} = 492$ Myr, equal to four bar revolution periods. However, the $m = 0$ component of the bar is included in models from the beginning. It can be interpreted as a pre-existing disc-like bulge (Athanassoula 2005). The mass of the bar, $M_b = 1.30 \times 10^{10}\,\mathrm{M}_\odot$, agrees with other estimates (e.g. Dwek et al. 1995).

Models include an exponential disc with scalelength R_d:

$$\Sigma = \Sigma_0 \mathrm{e}^{-R/R_d}, \tag{3}$$

where Σ and Σ_0 are the surface densities at radius R and the galactic centre, respectively. The velocity of the rotation curve, V_c, produced by an exponential disc is determined by the following relation:

$$V_c^2 = 4\pi G \Sigma_0 R_d y^2 [I_0(y)K_0(y) - I_1(y)K_1(y)], \tag{4}$$

where $y = 0.5R/R_d$, while I_n and K_n are modified Bessel functions of order n of the first and second kinds, respectively (Freeman 1970; Binney & Tremaine 1987).

Here the mass of the disc is chosen to be $M_d = 3.5 \times 10^{10}\,\mathrm{M}_\odot$. To compare this with the disc mass in N-body simulations, we should sum the mass of the disc and some part of that of the bar. The total value, 3.5–4.8 $\times\ 10^{10}\,\mathrm{M}_\odot$, is consistent with other estimates of the Galactic disc mass, 3.5–5.0 $\times\ 10^{10}\,\mathrm{M}_\odot$ (Shen et al. 2010; Fujii et al. 2019).

The classical bulge determines the potential in the galactic centre; it is modelled by a Plummer sphere (for example, Binney & Tremaine 1987), the rotation curve of which is defined by the following expression:

$$V_c^2(R) = \frac{G M_{bg} R^2}{(R^2 + R_{bg}^2)^{3/2}}, \tag{5}$$

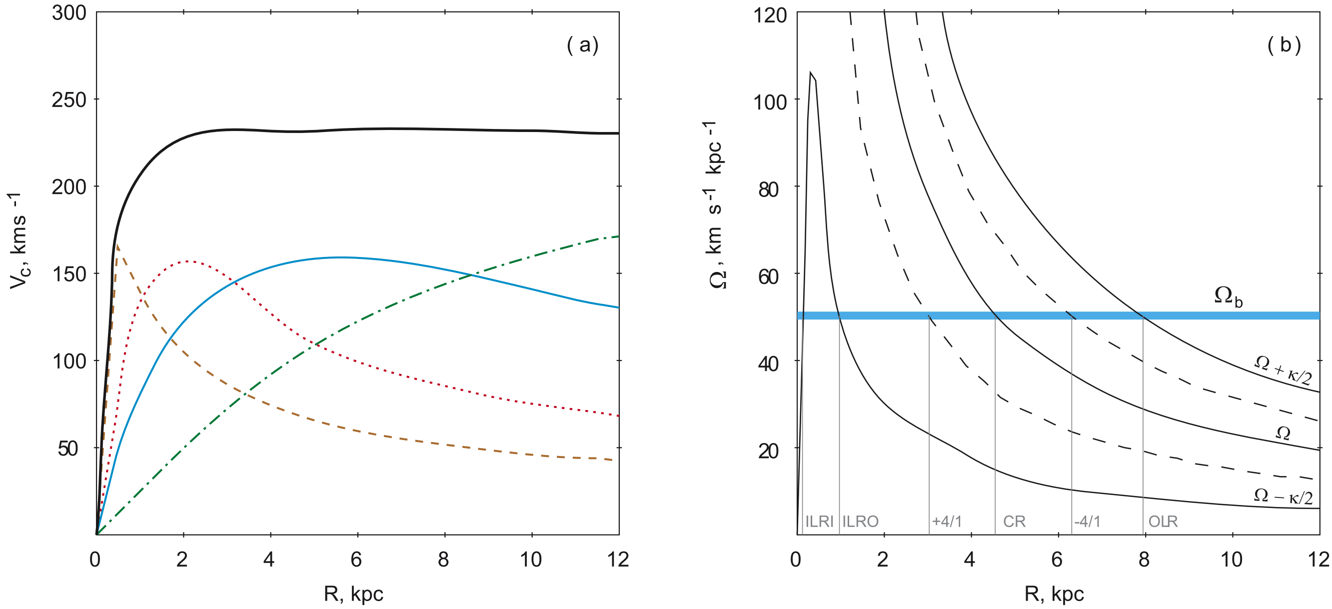

Figure 2. (a) Model rotation curves. The thick black line shows the total rotation curve while the dashed, dotted, solid and dash–dotted lines (coloured brown, red, blue and green in the online version of this article) indicate the contribution of the bulge, bar, disc and halo, respectively. (b) Dependence of the angular velocities on the galactocentric distance R. The continuous curves represent the angular velocities Ω and $\Omega \pm \kappa/2$, while the dashed lines indicate $\Omega \pm \kappa/4$. The horizontal thick line (coloured blue in the online article) shows the angular velocity of the bar, $\Omega_b = 50\,\mathrm{km\,s^{-1}\,kpc^{-1}}$. The resonance distances are determined by its intersections with the curves of angular velocities.

Table 3. Characteristics of models 1–4.

Model	Initial distribution	n	N_c
1	uniform within $R < 11$ kpc	$n = 2$	3.6×10^7
2	exponential, $r_d = 2.5$ kpc	$n = 2$	4.7×10^7
3	uniform within $R < 11$ kpc	$n = 2$	0
4	uniform within $R < 11$ kpc	$n = 1$	3.6×10^7

Table 4. Locations of the resonances.

Name	Definition	Models 1–3 R, kpc	Model 4 R, kpc
OLR	$\kappa/(\Omega - \Omega_b) = -2/1$	7.91	7.91
−4/1	$\kappa/(\Omega - \Omega_b) = -4/1$	6.29	6.29
CR	$\Omega = \Omega_b$	4.61	4.62
+ 4/1	$\kappa/(\Omega - \Omega_b) = 4/1$	3.01	2.92
ILRO	$\kappa/(\Omega - \Omega_b) = 2/1$	0.97	0.92
ILRI	$\kappa/(\Omega - \Omega_b) = 2/1$	0.13	0.13

where M_{bg} and R_{bg} are the mass and characteristic length of the bulge. The mass of the Galactic classical bulge is expected to lie in the range 3–6 × $10^9\,\mathrm{M_\odot}$ and the adopted value is $M_{bg} = 5 \times 10^9$ here (e.g. Dehnen & Binney 1998; Nataf 2017; Fujii et al. 2019).

The halo dominates on the galactic periphery. It is modelled as an isothermal sphere with the following rotation curve:

$$V_c^2(r) = V_{\max}^2 \frac{R^2}{R^2 + R_h^2}, \tag{6}$$

where $V_{\max}$ is the asymptotic maximum of the halo rotation curve and R_h is the core radius.

Fig. 2(a) shows the total rotation curve produced by the gravitation of the bulge, bar, disc and halo. The total rotation curve

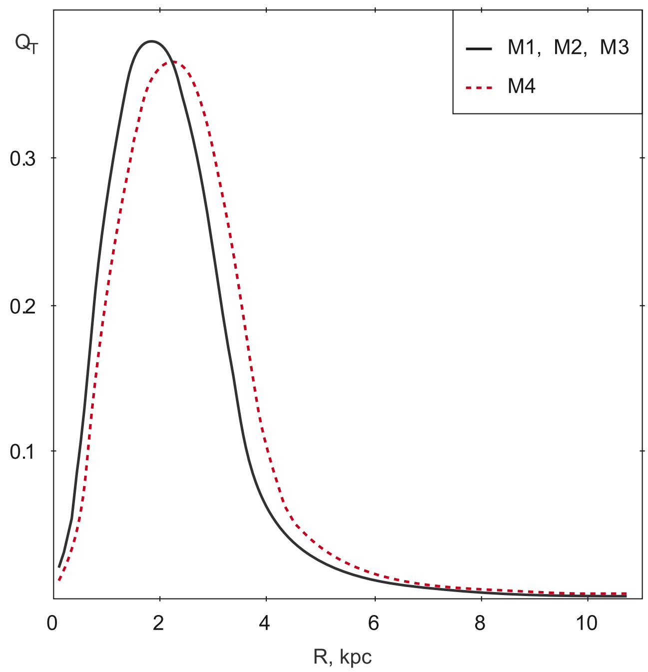

Figure 3. Variations of the parameter Q_T with galactic radius, R, in models 1–3 and in model 4. The power index n equals $n = 2$ and $n = 1$ in models 1–3 and model 4, respectively, while other parameters which determine the potential are the same. The maximal value of Q_T amounts to 0.380 in models 1–3 and to 0.367 in model 4. However, at the distance of the OLR, 7.9 kpc, the value of Q_T is larger in model 4 ($Q_T = 0.0074$) than in models 1–3 ($Q_T = 0.0057$).

is nearly flat, with an average azimuthal velocity of $\Theta = 232$ km $\mathrm{s^{-1}}$. This model value corresponds to an angular velocity at the solar distance ($R_0 = 7.5$ kpc) of $\Omega_0 = 30.9\,\mathrm{km\,s^{-1}\,kpc^{-1}}$ and is consistent with observations, $\Omega_0 = 31 \pm 1\,\mathrm{km\,s^{-1}\,kpc^{-1}}$(Melnik &

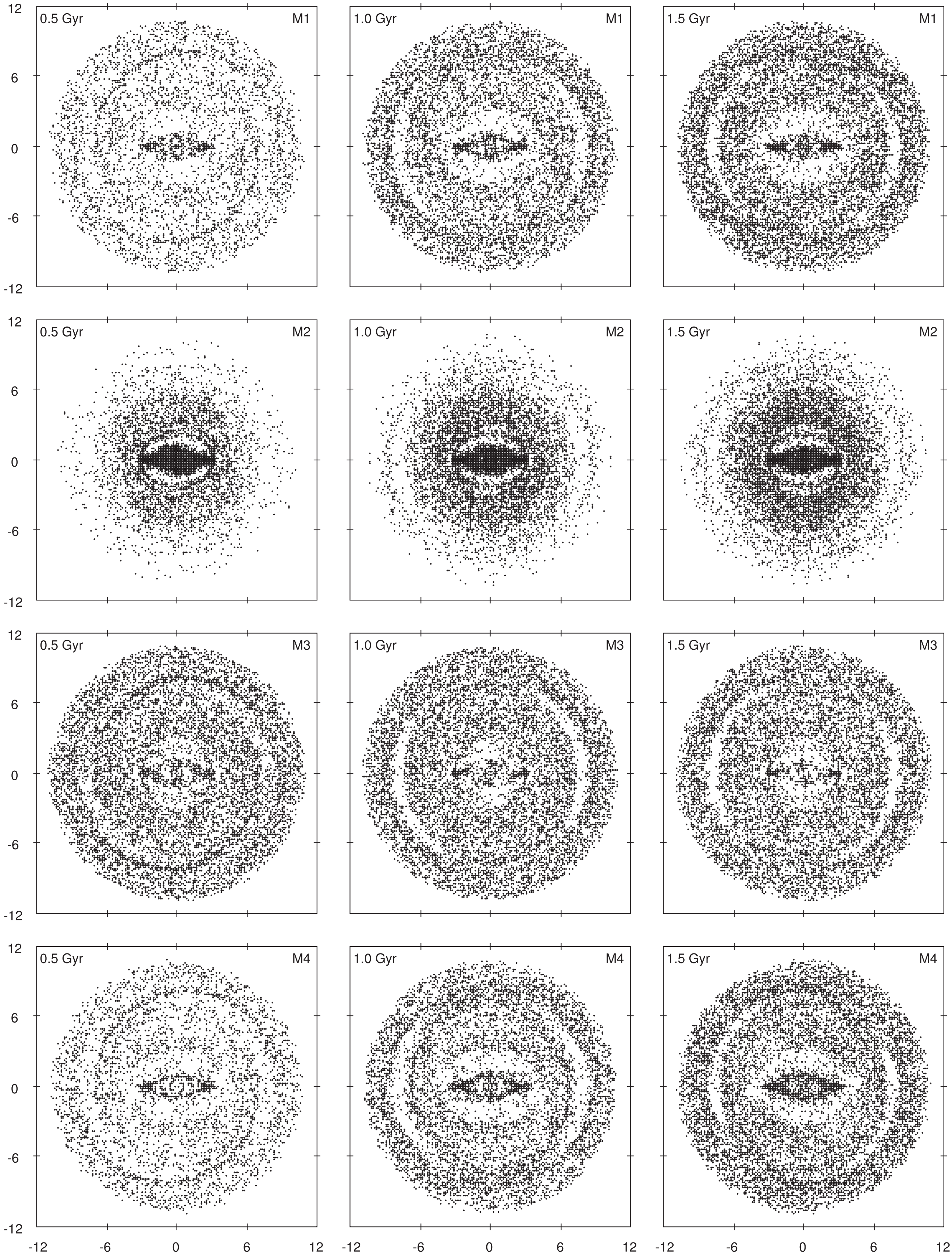

Figure 4. Distribution of model particles at three time moments: 0.5, 1.0 and 1.5 Gyr. Frames related to models 1, 2 and 4 display the distribution of OB particles, while those for model 3 demonstrate the distribution of 10 per cent of collisionless particles. The size of the frames is 24×24 kpc^2.

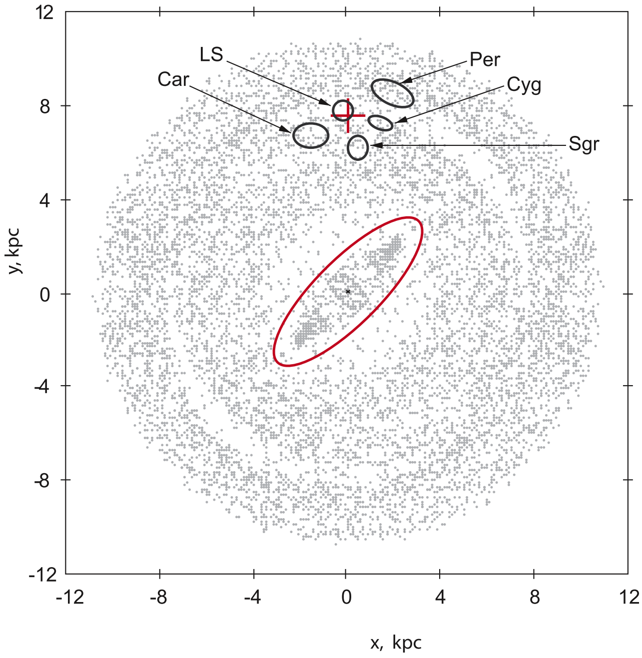

Figure 5. Distribution of OB particles (grey points) in the galactic plane. Also shown are the boundaries of the following star-gas complexes: Sagittarius, Carina, Cygnus, Local System (LS) and Perseus. Model 1 at $t = 1.5$ Gyr is considered. The position of the Sun is indicated by a large cross. The location of the Ferrers ellipsoid is also marked. The position angle of the Sun with respect to the bar is supposed to be $\theta_b = 45°$. As our Galaxy is traditionally considered to rotate clockwise (i.e. as if being observed from the North Galactic Pole), the model galaxy is also set to rotate clockwise. The Sagittarius, Carina, Cygnus and LS complexes lie in the vicinity of the outer ring R_1, but the Perseus complex is related to the outer ring R_2.

Dambis 2017, in preparation). Model and observed rotation curves are in good agreement with each other, at least in the 3-kpc solar neighbourhood.

Fig. 2(b) demonstrates the positions of the resonances, which correspond to the intersections of the horizontal line indicating the angular velocity of the bar ($\Omega_b = 50\,\mathrm{km\ s^{-1}\ kpc^{-1}}$) with the appropriate curves of angular velocity. Note that the present models include two inner Lindblad resonances (ILRs): outer (ILRO) and inner (ILRI) ones. The CR of the bar lies at a radius of 4.6 kpc near the end of the Ferrers ellipsoid ($a = 4.2$ kpc), so the model bar is dynamically fast (Debattista & Sellwood 2000; Rautiainen, Salo & Laurikainen 2008).

The models can be rescaled for slightly different values of the solar Galactocentric distance R_0. This is possible due to the fact that the Galactic rotation curve is flat in the solar neighbourhood. If the ratio of the new and old values of R_0 is $q = (R_{\mathrm{new}}/R_{\mathrm{old}})$, then the masses of the bulge, bar and disc must be changed by a factor of $\sim q^2$, but the asymptotic velocity of the halo by a factor of $\sim q$. The new rotation curve will also be flat in the solar neighbourhood.

If test particles approach each other at a small distance, ε, they can collide with each other inelastically, imitating the behaviour of a gas subsystem (Brahic & Henon 1977; Levinson & Roberts 1981; Roberts & Hausman 1984). Collisions are assumed to be absolutely inelastic, so the velocities of two gas particles after a collision are the same, $\boldsymbol{v}'_1 = \boldsymbol{v}'_2$ equal to $(\boldsymbol{v}_1 + \boldsymbol{v}_2)/2$, where $\boldsymbol{v}$ and $\boldsymbol{v}'$ are the velocities before and after a collision, respectively.

The changes of velocities due to collisions at each step are performed before leapfrog integration. To accelerate the computation of collisions, we sort particles in ascending order of the coordinate x at each step of integration, as supposed by Salo (1991).

There is a danger that a pair of gas particles can fall into 'permanent collisions' (Brahic & Henon 1977), i.e. the same two particles would collide at each step of integration. Galactic differential rotation can tear some close pairs of colliding particles apart, but it is powerless for particles lying at the same galactic radius. The main remedy against 'permanent collisions' is quite large velocity dispersion in the radial direction, maintained above some minimal level, $\sigma_{\min}$, throughout the galactic disc. 'Permanent collisions' can be avoided if the average distance passed by a particle relative to another during one step of integration Δt is always larger than the length of collision, ε:

$$\sqrt{2}\sigma_{\min}\Delta t \geq \varepsilon. \tag{7}$$

Epicyclic motions and perturbations from the bar increase the velocity dispersion, while collisions decrease it. The parameter ε regulates the frequency of collisions, which grows with increasing ε. The choice of the initial velocity dispersion σ_0 equal to $5\,\mathrm{km\ s^{-1}}$ and an ε value of 0.05 pc (Table 2) ensures the velocity dispersion, σ_R, never drops below $5\,\mathrm{km\ s^{-1}}$, so condition (7) is always fulfilled (see also Section 4.4).

Two colliding gas particles have a probability, P_c, that one of them forms an OB association that will not take part in collisions during some time interval, t_{ob}. OB particles move ballistically, but after time t_{ob} they transform back into gas particles, resuming their ability to collide (Roberts & Hausman 1984; Salo 1991). The interest in OB particles is due to the fact that they indicate the places with the highest density of model particles and outline the positions of different morphological structures. Generally, OB particles imitate the process of formation of OB associations only roughly. Values of P_{ob} and t_{ob} are usually taken to be 10 per cent and 4 Myr, respectively (Table 2).

The initial surface density of model particles in model 1 is uniform within the radius $R < 11$ kpc (Table 2).

Model 1 is a basic model of our study. However, we also consider three other models, which differ from model 1 in one of the following features: the initial distribution, presence/absence of collisions and power index n of the density distribution inside the Ferrers ellipsoid. Model 2 starts from an exponential distribution of gas particles in the galactic plane with a scalelength of $r_d = 2.5$ kpc, but values of all other parameters coincide with those of model 1. Model 3 is collisionless and that is its only difference from model 1. Model 4 includes the Ferrers bar, the density distribution of which is determined by the power index $n = 1$, i.e. its bar is less centrally concentrated than in other models, but the mass of the bar, M_b, and all other parameters are the same as in model 1. Table 3 briefly characterizes models 1–4 and presents the total number of collisions, N_c, that occurred during the simulation time.

All models considered have the same angular velocity of the bar, $\Omega_b = 50\,\mathrm{km\ s^{-1}\ kpc^{-1}}$. As the distribution of the potential is the same in models 1–3, the locations of the resonances must also be the same there. Formally, model 4 differs from models 1–3 in its potential distribution, but that affects the positions of the resonances weakly. Table 4 presents the resonance locations in models 1–3 and in model 4. It is seen that the difference in the resonance radii does not exceed 0.1 kpc and mainly concerns the ILRO and +4/1 resonance, but the radius of the OLR is the same in all models considered.

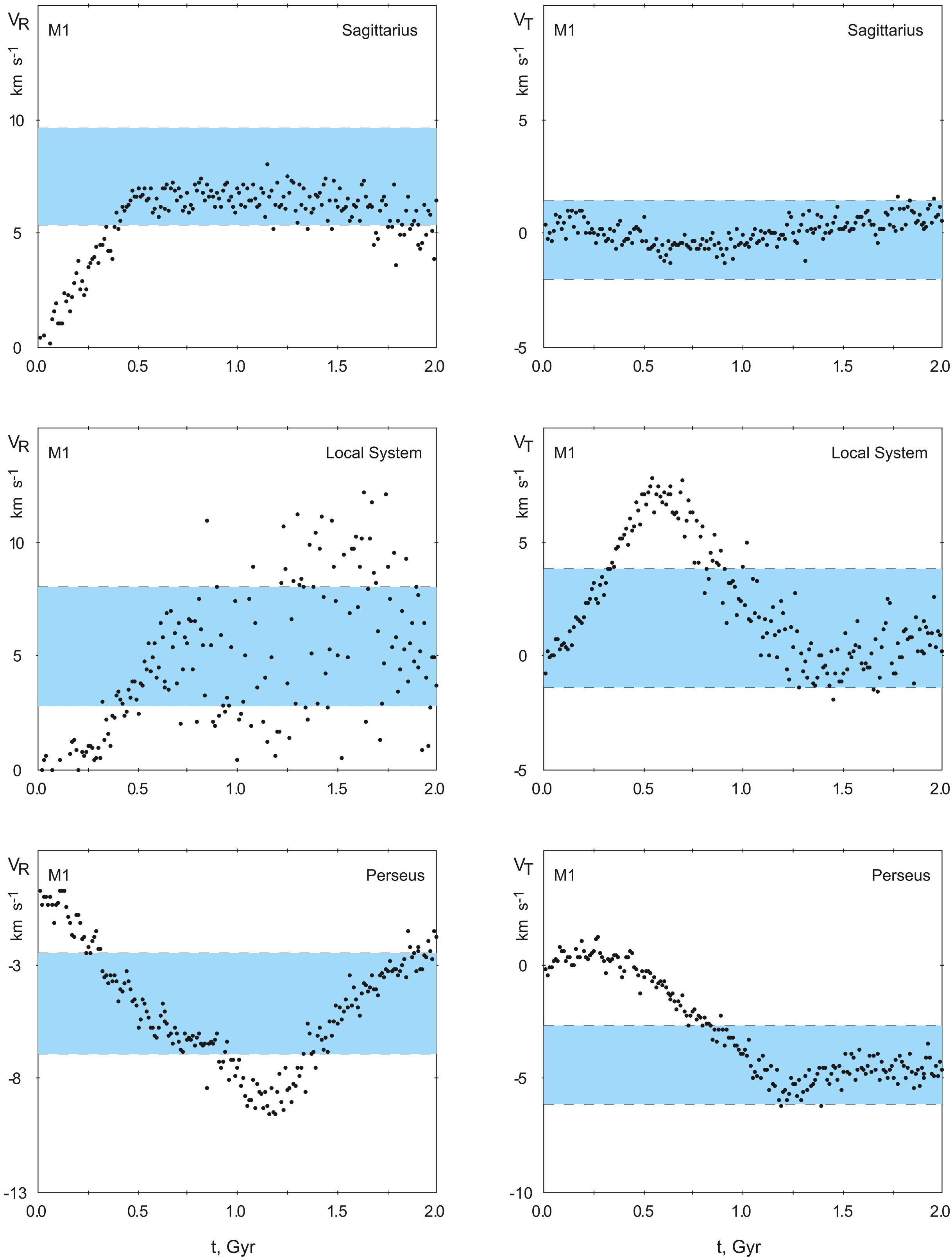

Figure 6. Comparison of model and observed residual velocities calculated for three star-gas complexes: Sagittarius, Local System and Perseus. The left and right panels show radial and azimuthal ($V_{\rm R}$ and $V_{\rm T}$) residual velocities, respectively. The grey strips (coloured blue in the online article) display the uncertainties in determination of the observed residual velocities, $V_{\rm obs} \pm \varepsilon_v$ (Table 1). Black circles indicate the average velocities of model particles (gas + OB) located inside the boundaries of star-gas complexes in model 1 every 10 Myr. The position angle of the Sun with respect to the bar is adopted as $\theta_{\rm b} = 45°$.

Table 5. Residual velocities, V_R and V_T, calculated for the Sagittarius, Local System and Perseus star-gas complexes in models 1–4.

Complex		Sagittarius			Local System			Perseus		
Model	t Gyr	V_R km s^{-1}	V_T km s^{-1}	n	V_R km s^{-1}	V_T km s^{-1}	n	V_R km s^{-1}	V_T km s^{-1}	n
Model 1	0.7	6.6 ± 0.1	− 0.5 ± 0.1	178	5.1 ± 0.3	6.2 ± 0.2	186	− 6.0 ± 0.1	− 1.9 ± 0.1	378
	0.9	6.7 ± 0.1	− 0.5 ± 0.1	183	4.1 ± 0.7	3.4 ± 0.2	145	− 6.9 ± 0.2	− 3.1 ± 0.1	434
	1.1	6.6 ± 0.1	− 0.2 ± 0.1	182	2.5 ± 0.7	1.7 ± 0.3	103	− 8.8 ± 0.1	− 4.8 ± 0.2	488
	1.3	6.5 ± 0.1	0.2 ± 0.1	184	6.5 ± 0.7	− 0.0 ± 0.2	77	− 7.7 ± 0.2	− 5.3 ± 0.1	479
	1.5	6.3 ± 0.1	0.4 ± 0.1	182	7.4 ± 0.9	− 0.3 ± 0.2	74	− 5.3 ± 0.2	− 4.6 ± 0.1	457
	1.7	5.9 ± 0.2	0.6 ± 0.1	184	7.4 ± 0.7	0.1 ± 0.3	79	− 3.7 ± 0.1	− 4.5 ± 0.1	452
	1.9	5.4 ± 0.2	0.8 ± 0.1	191	5.0 ± 0.5	0.8 ± 0.2	94	− 2.6 ± 0.1	− 4.6 ± 0.1	449
M2	0.7	6.9 ± 0.1	− 0.6 ± 0.1	168	5.8 ± 0.4	5.5 ± 0.2	88	− 6.6 ± 0.2	− 2.2 ± 0.1	116
	0.9	6.7 ± 0.2	− 0.4 ± 0.1	165	4.9 ± 0.9	2.7 ± 0.2	69	− 8.3 ± 0.3	− 3.8 ± 0.1	143
	1.1	6.3 ± 0.1	− 0.3 ± 0.1	166	2.5 ± 0.7	0.9 ± 0.3	49	− 10.3 ± 0.2	− 5.8 ± 0.2	157
	1.3	6.2 ± 0.1	− 0.1 ± 0.1	173	7.4 ± 1.4	− 1.0 ± 0.3	38	− 9.7 ± 0.3	− 6.7 ± 0.2	163
	1.5	6.2 ± 0.1	0.2 ± 0.1	172	8.4 ± 1.0	− 1.4 ± 0.3	34	− 5.7 ± 0.3	− 5.9 ± 0.2	147
	1.7	5.8 ± 0.2	0.6 ± 0.1	170	7.9 ± 0.8	− 1.0 ± 0.4	39	− 3.8 ± 0.2	− 6.1 ± 0.2	148
	1.9	5.2 ± 0.1	0.6 ± 0.1	175	6.6 ± 0.5	− 0.3 ± 0.2	46	− 1.7 ± 0.2	− 6.1 ± 0.2	150
M3	0.7	6.6 ± 0.1	− 0.3 ± 0.1	182	5.9 ± 0.3	5.8 ± 0.3	182	− 5.8 ± 0.1	− 1.8 ± 0.1	372
	0.9	6.5 ± 0.1	− 0.3 ± 0.1	184	4.4 ± 0.8	3.2 ± 0.2	144	− 6.9 ± 0.2	− 3.1 ± 0.1	429
	1.1	6.7 ± 0.1	0.0 ± 0.1	180	2.9 ± 0.6	0.7 ± 0.2	104	− 8.8 ± 0.2	− 4.6 ± 0.1	475
	1.3	6.4 ± 0.1	0.2 ± 0.1	185	6.0 ± 0.8	− 0.6 ± 0.3	74	− 8.0 ± 0.2	− 5.2 ± 0.1	462
	1.5	6.2 ± 0.1	0.7 ± 0.1	185	9.0 ± 0.7	− 1.1 ± 0.2	71	− 5.0 ± 0.2	− 4.6 ± 0.1	439
	1.7	5.8 ± 0.2	1.1 ± 0.1	190	7.4 ± 0.4	− 0.4 ± 0.2	78	− 3.4 ± 0.1	− 4.6 ± 0.1	441
	1.9	5.2 ± 0.2	1.2 ± 0.1	190	5.8 ± 0.3	0.1 ± 0.2	93	− 2.0 ± 0.1	− 4.8 ± 0.1	441
M4	0.7	8.4 ± 0.2	− 0.7 ± 0.1	174	6.6 ± 0.5	5.4 ± 0.3	171	− 8.3 ± 0.2	− 2.9 ± 0.1	385
	0.9	8.2 ± 0.1	− 0.1 ± 0.1	175	4.4 ± 0.8	2.7 ± 0.3	122	− 10.3 ± 0.2	− 4.9 ± 0.2	470
	1.1	8.2 ± 0.2	0.6 ± 0.1	181	4.5 ± 0.8	0.2 ± 0.3	74	− 9.8 ± 0.3	− 5.8 ± 0.1	475
	1.3	7.7 ± 0.2	1.1 ± 0.1	191	11.1 ± 0.7	− 1.6 ± 0.4	60	− 5.7 ± 0.2	− 4.8 ± 0.1	427
	1.5	6.6 ± 0.2	1.5 ± 0.1	194	8.6 ± 0.7	− 0.6 ± 0.2	67	− 3.9 ± 0.2	− 4.9 ± 0.1	447
	1.7	5.4 ± 0.2	1.3 ± 0.2	188	4.8 ± 0.6	1.3 ± 0.2	88	− 2.9 ± 0.2	− 5.1 ± 0.1	437
	1.9	5.2 ± 0.2	0.7 ± 0.1	192	2.5 ± 0.4	2.2 ± 0.2	128	− 3.7 ± 0.2	− 4.0 ± 0.1	409
Observations		7.5 ± 2.1	− 0.3 ± 1.7		5.4 ± 2.6	1.2 ± 2.6		− 4.7 ± 2.2	− 4.4 ± 1.7	

The amount of non-axisymmetric perturbations produced by the bar is usually estimated through the parameter $Q_T(R)$, which is the ratio of the maximal tangential force at some radius to the azimuthally average radial force at the same radius:

$$Q_T(R) = \frac{\max(|F_T|)}{<|F_R|>}. \quad (8)$$

The value of Q_T varies with radius. Its maximal value is named Q_b and is usually used as a measure of the strength of the bar:

$$Q_b = \max[Q_T(R)] \quad (9)$$

(Sanders & Tubbs 1980; Combes & Sanders 1981; Athanassoula et al. 1983).

Fig. 3 shows the variations of Q_T with galactic radius calculated for models 1–3 and for model 4. Maximal values of Q_T are 0.380 (models 1–3) and 0.367 (model 4). They are achieved at distances of 1.8 and 2.2 kpc, respectively. The value of the bar strength $Q_b \approx 0.38$ agrees with expectations for galaxies with strong bars (Block et al. 2001; Buta, Laurikainen & Salo 2004; Díaz-García et al. 2016). Note that at the distance of the OLR, $R = 7.9$ kpc, the value of Q_T is larger in model 4 ($Q_T = 0.0074$) than in models 1–3 ($Q_T = 0.0057$) by 25 per cent. This small preponderance of model 4 being amplified by the resonance results in larger velocity perturbations produced by model 4 in the solar neighbourhood.

The value of the bar strength, Q_b, is sensitive to the choice of bulge mass: the larger M_{bg}, the smaller Q_T. For example, the increase of M_{bg} from 5 to 9 × 10^9 $M_\odot$ results in the decrease of Q_b from 0.38 to 0.34.

Fig. 4 shows the distribution of model particles at three time moments: 0.5, 1.0 and 1.5 Gyr. The frames related to models 1, 2 and 4 demonstrate the distribution of OB particles. Model 3 is collisionless, so OB particles are not forming there; the corresponding frames merely present the distribution of 10 per cent of model particles. We can see that model discs form nuclear rings (∼0.5 kpc) and conspicuous outer rings R_2 (∼9.0 kpc). Model galaxies also produce outer rings R_1 (∼6 kpc) and inner rings (∼3 kpc), which are noticeable mainly in the density profiles (Section 4.3). Note that all models demonstrate diamond-shape structures that are located inside the Ferrers ellipsoids and indicate the locations of the most densely populated bar orbits. These structures are not inner rings, which usually have more round shapes and form outside the bar. Model 2 (t = 0.5 Gyr) gives a good example of an inner ring that touches the bar only at the bar ends. Models 1 and 3 also include inner rings, but they are hardly visible in Fig. 4 (see Section 4.3). The nuclear and inner rings form quickly and are already in existence at time t = 0.5 Gyr, when the bar acquires its full strength. The outer rings grow more slowly: they appear as pseudorings at t = 0.5 Gyr and take a pure elliptical shape at time $t \approx 1.0$ Gyr. Once formed, the outer rings exist to the end of the simulation.

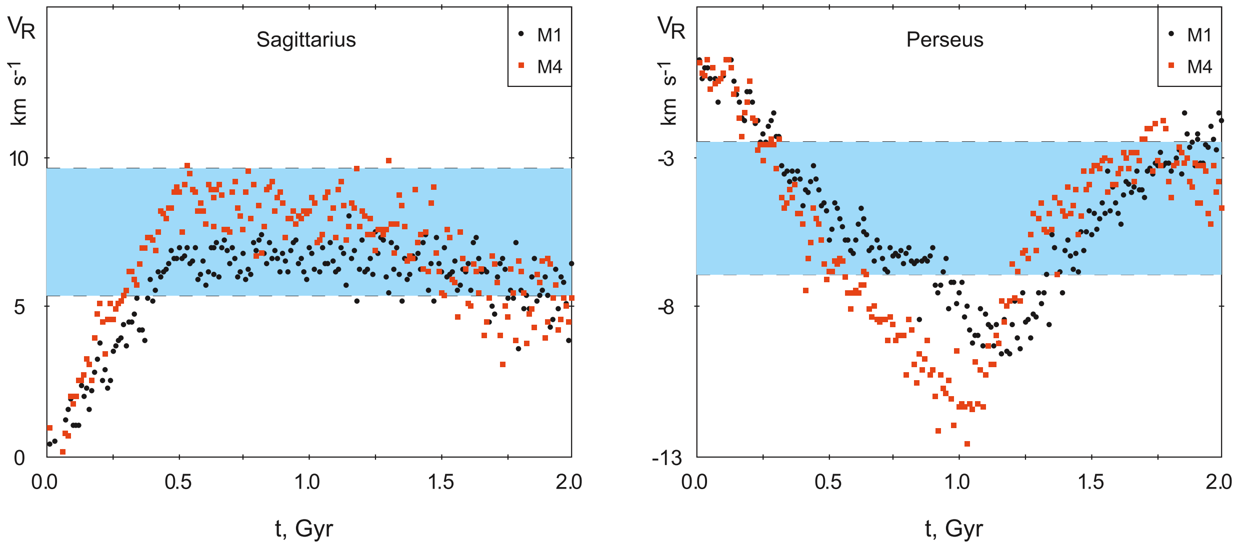

Figure 7. Variations of the radial residual velocity $V_{\rm R}$ in the Sagittarius and Perseus complexes in models 1 and 4. The absolute values of the velocities $V_{\rm R}$ are larger in model 4 than in model 1, which can be connected with the larger value of $Q_{\rm T}$ in model 4 than in model 1 in the solar neighbourhood.

4 RESULTS

4.1 Kinematics of model particles in the solar neighbourhood

The epicyclic motions of model particles located near the OLR of the bar are adjusted in accordance with the perturbations coming from the bar that result in the formation of conspicuous systematic velocities.

Fig. 5 shows the distribution of OB particles in the galactic plane in model 1 at t = 1.5 Gyr and the boundaries of the Sagittarius, Carina, Cygnus, Local System (LS) and Perseus star-gas complexes. Model velocities in the star-gas complexes are calculated as average velocities of model particles (gas + OB) located inside the boundaries of the complexes at the moment considered. The model residual velocities are determined with respect to the model rotation curve. The velocities in the complexes are derived every 10 Myr. Note that, at every moment considered, the boundaries of the complexes include different sets of model particles, but the position of the boundaries with respect to the bar major axis remains the same, corresponding to the solar position angle $\theta_{\rm b} = 45^\circ$ (see Section 4.2).

Fig. 6 demonstrates the residual velocities in the Sagittarius, Local System and Perseus star-gas complexes computed for model 1 at different time moments. We can see that the scatter of model velocities is quite small (0.3–1.0 km s^{-1}) everywhere except for $V_{\rm R}$ velocities in the Local System, where it amounts to 3–4 km s^{-1}. The Local System is located between two outer rings and includes particles related to both of them: R_1 objects have positive radial velocities, while R_2 objects have negative ones (see also Fig. 15 later). Though the scatter of velocities $V_{\rm R}$ in the Local System is quite large, their average value is close to the observed one, $V_{\rm R} = 5.4$ km s^{-1} (Table 1).

Table 5 lists the average values of the model residual velocities, $V_{\rm R}$ and $V_{\rm T}$, in the three star-gas complexes computed for seven time intervals: 0.6–0.8, 0.8–1.0, 1.0–1.2, 1.2–1.4, 1.4–1.6, 1.6–1.8 and 1.8–2.0 Gyr, each of which includes 20 instantaneous estimates. It also presents the average time from the start of simulations to the interval considered, t, and the average number of model particles, n, that appear to be inside the boundaries of the complexes. The last line indicates the observed residual velocities in the corresponding complexes.

Fig. 6 and Table 5 suggest that there are many time moments when the model and observed velocities in the three star-gas complexes agree within the errors. The Sagittarius complex demonstrates good agreement between model and observed velocities in the time interval 0.3–1.8 Gyr. In the Local System, the situation is more complicated: the model and observed radial velocities, $V_{\rm R}$, are consistent within the errors in 75 per cent of time moments from the interval 0.5–2.0 Gyr, but the azimuthal velocities, $V_{\rm T}$, agree in the interval 0.8–2.0 Gyr. The Perseus complex shows a good accordance between model and observed radial velocities, $V_{\rm R}$, for two time intervals, 0.5–1.0 and 1.4–1.8 Gyr, while an agreement in azimuthal velocities, $V_{\rm T}$, is reached for the time interval 1.0–2.0 Gyr. Hereafter, t = 1.5 Gyr will be regarded as a reference time moment at which model and observed velocities in the Sagittarius, Local System and Perseus star-gas complexes are in good agreement.

Table 5 indicates that the residual velocities, $V_{\rm R}$ and $V_{\rm T}$, produced by models 1–3 are nearly the same, while model 4 creates slightly larger velocity perturbations. This difference is especially noticeable in the distribution of velocities $V_{\rm R}$ in the Sagittarius and Perseus complexes. To compare models 1 and 4, we build Fig. 7, which shows the radial residual velocities $V_{\rm R}$ produced by both models in the Sagittarius and Perseus complexes. The absolute values of the radial velocities $V_{\rm R}$ are larger in model 4 than in model 1, which could be connected with the larger value of $Q_{\rm T}$ in model 4 than in model 1 in the solar neighbourhood (Fig. 3).

Fig. 8 shows the distribution of OB particles with negative ($V_{\rm res} < 5$ km s^{-1}) and positive ($V_{\rm res} > 5$ km s^{-1}) residual velocities in model 1 at t = 1.5 Gyr. Particles with residual velocities close to zero ($|V_{\rm res}| < 5$ km s^{-1}) are not shown there. The left panel indicates that velocities $V_{\rm R}$ of model particles are positive in the Sagittarius, Carina, Cygnus and Local System star-gas complexes, while they are negative in the Perseus complex. The right panel shows that velocities $V_{\rm T}$ are negative in the Perseus complex.

Fig. 9 demonstrates the variations of radial velocity $V_{\rm R}$ with distance R calculated for five radius vectors connecting the Galactic Centre with the centres of the corresponding star-gas complexes: Sagittarius, Carina, Cygnus, Local System and Perseus. These

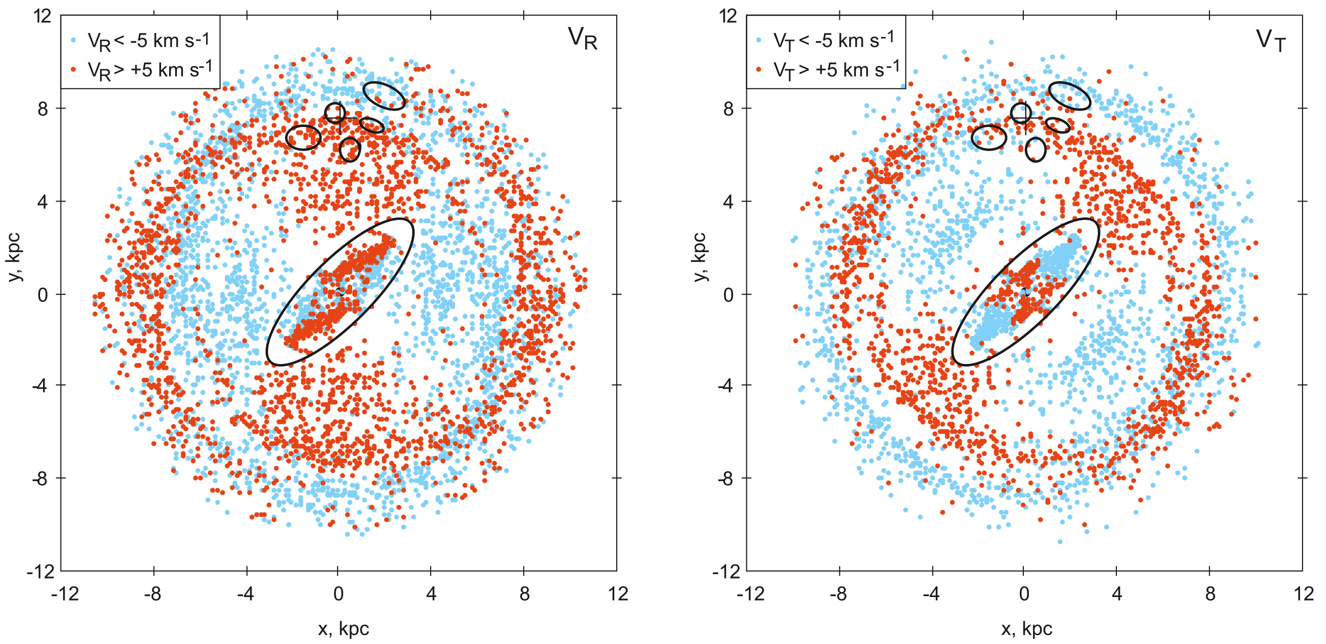

Figure 8. Distribution of OB particles with negative and positive residual velocities in model 1 at $t = 1.5$ Gyr. The left and right panels represent the distribution of radial, V_R, and azimuthal, V_T, residual velocities, respectively. Particles with conspicuous positive velocities ($V_R > +5$ or $V_T > +5\,\mathrm{km\,s^{-1}}$) are indicated as dark-grey circles (coloured red in the online article), while those with conspicuous negative velocities ($V_R < -5$ or $V_T < -5\,\mathrm{km\,s^{-1}}$) are shown as light-grey circles (coloured blue in the online article). Particles with residual velocities close to zero ($|V_R| < 5$ or $|V_T| < 5\,\mathrm{km\,s^{-1}}$) are not shown here. It also represents the boundaries of the Sagittarius, Carina, Cygnus, LS and Perseus star-gas complexes. The model galaxy is turned to rotate clockwise. The location of the complexes is determined for the solar position angle of $\theta_b = 45°$. The left panel indicates that the velocities V_R of model particles are positive in the Sagittarius, Carina, Cygnus and LS star-gas complexes, while they are negative in the Perseus complex. The right panel shows that the velocities V_T are negative in the Perseus complex.

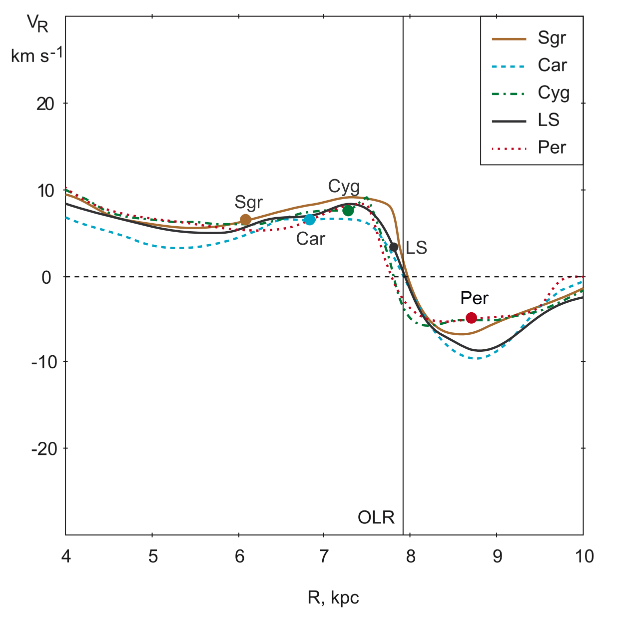

Figure 9. Variations of radial residual velocities, V_R, with Galactocentric distance, R, calculated for five Galactic radius vectors connecting the Galactic Centre with the centres of the corresponding star-gas complexes: Sagittarius, Carina, Cygnus, Local System and Perseus. The position angle of the Sun with respect to the bar major axis is $\theta_b = 45°$. The vertical line indicates the radius of the OLR. The model velocity V_R at each point of the profiles is computed as the average velocity of model particles (gas + OB) located inside a small region with radius 0.5 kpc and a centre lying on the corresponding radius vector. Model 1 at $t = 1.5$ Gyr is considered. All profiles demonstrate a sharp drop in velocity V_R at the distance of the OLR.

radius vectors form slightly different angles with the Sun–Galactic Centre line: $\theta = 4.0°$ (Sgr), $-13.3°$ (Car), $+11.0°$ (Cyg), $-1.6°$ (LS) and 12.8° (Per). The velocity V_R at each point of the profiles is computed as the average velocity of model particles (gas + OB) located inside a small circle with radius 0.5 kpc and a centre lying on the corresponding radius vector. Model 1 at $t = 1.5$ Gyr is considered. It is clear that all profiles demonstrate a sharp drop in the velocity V_R at the distance of the OLR. Generally, we can shift the position of the OLR of the bar by choosing a different value of Ω_b, but if we want the velocity V_R in the Local System to be positive, then we will inevitably obtain positive V_R in the Sagittarius, Carina and Cygnus complexes, which are located at smaller Galactocentric distances R than the Local System. However, the observed velocities V_R in the Carina and Cygnus complexes are negative (Table 1).

The uncertainty in the choice of value of the angular velocity of the bar, $\Omega_b = 50\,\mathrm{km\,s^{-1}\,kpc^{-1}}$, is less than $\pm 2\,\mathrm{km\,s^{-1}\,kpc^{-1}}$. If we choose Ω_b to be $52\,\mathrm{km\,s^{-1}\,kpc^{-1}}$, then the radius of the OLR will be shifted by 0.3 kpc toward the Galactic Centre and the average velocities V_R in the Local System will be negative. In contrast, the value of $\Omega_b = 48\,\mathrm{km\,s^{-1}\,kpc^{-1}}$ shifts the OLR by 0.3 kpc away from the Galactic Centre and causes the velocities V_T in the Perseus region to be too small in absolute value, $|V_T| < 3\,\mathrm{km\,s^{-1}}$. All these changes cause a discrepancy with observations.

Table 6 lists the average residual velocities of model particles, V_R and V_T, located within the boundaries of the Carina and Cygnus star-gas complexes in model 1 at different time moments. Other models give similar results. The bottom line indicates the observed velocities. It is clear that the present models cannot reproduce the observed velocities in the Carina and Cygnus complexes. Probably some important physical processes that

Table 6. Residual velocities, V_R and V_T, computed for the Carina and Cygnus star-gas complexes in model 1.

Complex	Carina			Cygnus		
t Gyr	V_R km s^{-1}	V_T km s^{-1}	n	V_R km s^{-1}	V_T km s^{-1}	n
0.7	6.1 ± 0.1	− 2.5 ± 0.2	282	8.2 ± 0.2	9.0 ± 0.1	217
0.9	6.3 ± 0.1	0.6 ± 0.3	326	7.1 ± 0.4	8.9 ± 0.3	153
1.1	5.8 ± 0.1	3.0 ± 0.2	345	6.2 ± 0.4	6.7 ± 0.3	110
1.3	5.9 ± 0.2	2.2 ± 0.2	320	7.4 ± 0.4	4.1 ± 0.3	106
1.5	5.9 ± 0.1	0.2 ± 0.2	304	8.9 ± 0.3	3.0 ± 0.2	103
1.7	6.5 ± 0.1	− 1.1 ± 0.1	291	9.4 ± 0.4	2.9 ± 0.1	100
1.9	6.7 ± 0.2	− 1.2 ± 0.2	282	9.5 ± 0.3	2.5 ± 0.2	96
Observations	− 6.2 ± 2.6	+6.2 ± 2.8		− 4.3 ± 1.3	− 10.3 ± 1.4	

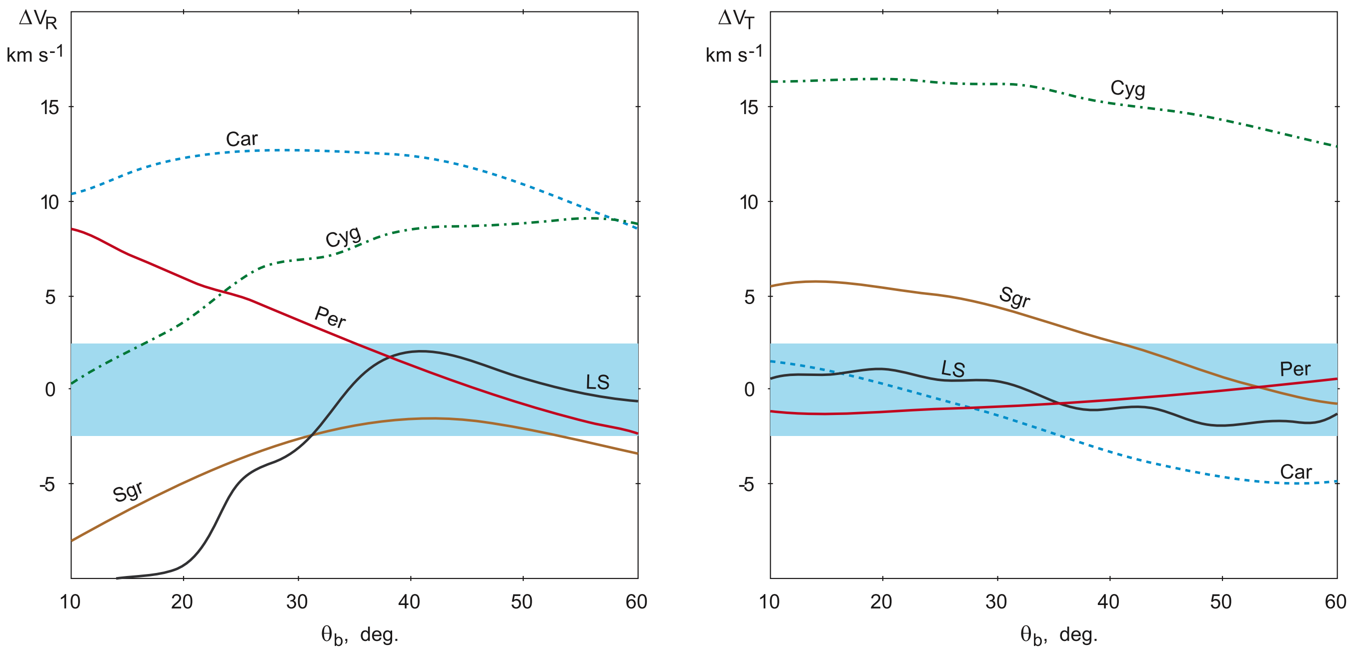

Figure 10. Dependence of the differences between model and observed velocities, ΔV_R and ΔV_T, on the position angle θ_b of the bar calculated for five star-gas complexes: Sagittarius, Carina, Cygnus, Local System (LS) and Perseus. The left and right panels show variations of the radial and azimuthal, V_R and V_T, residual velocities, respectively. The grey strips (coloured blue in the online article) display the permissable intervals of deviations between model and observed velocities, which are chosen to be ±2.5 km s^{-1}. If a curve indicating values of ΔV_R or ΔV_T in some complex lies inside the strip, then model and observed velocities are consistent within the errors there.

determine the kinematics in these two regions are not included in consideration.

4.2 Position angle of the Sun with respect to the bar major axis

In the previous analysis, the value of the position angle of the Sun with respect to the bar major axis was adopted as $\theta_b = 45°$. This section gives some rationale for that choice. Fig. 10 shows the dependence of the difference between model and observed residual velocities, ΔV_R and ΔV_T,

$$\Delta V_R = V_{R\,\mathrm{mod}} - V_{R\,\mathrm{obs}}, \qquad (10)$$

$$\Delta V_T = V_{T\,\mathrm{mod}} - V_{T\,\mathrm{obs}}, \qquad (11)$$

on the position angle θ_b. The model residual velocities are determined as average residual velocities in model 1 in the time interval 1.4–1.6 Gyr. The strips show the intervals of permissable deviations between model and observed velocities, which are chosen to be ±2.5 km s^{-1}, representing the average uncertainty in determination of observed velocities (Table 1). If a curve indicating values of ΔV_R or ΔV_T in some complex lies inside the corresponding strip, then the model and observed velocities are consistent within the errors there.

Fig. 10 (left panel) demonstrates that model and observed velocities V_R in the Sagittarius, LS and Perseus star-gas complexes agree within the errors for position angle θ_b lying in the range 33–52°. Note that the best agreement between model and observed velocities V_R in the Sagittarius complex corresponds to $\theta_b \approx 45°$. The Carina and Cygnus complexes show a large discrepancy between model and observed velocities for all values of θ_b from the interval considered.

The most interesting feature in variations of the azimuthal velocity V_T concerns the Sagittarius complex. Fig. 10 (right panel) indicates that model and observed velocities V_T in the Sagittarius complex are consistent within the errors for $\theta_b > 40°$. In contrast, the curve built for the Carina complex suggests that model and observed velocities agree for $\theta_b < 40°$ there. Note that model velocities V_T in the Local System and Perseus complexes are not sensitive to the

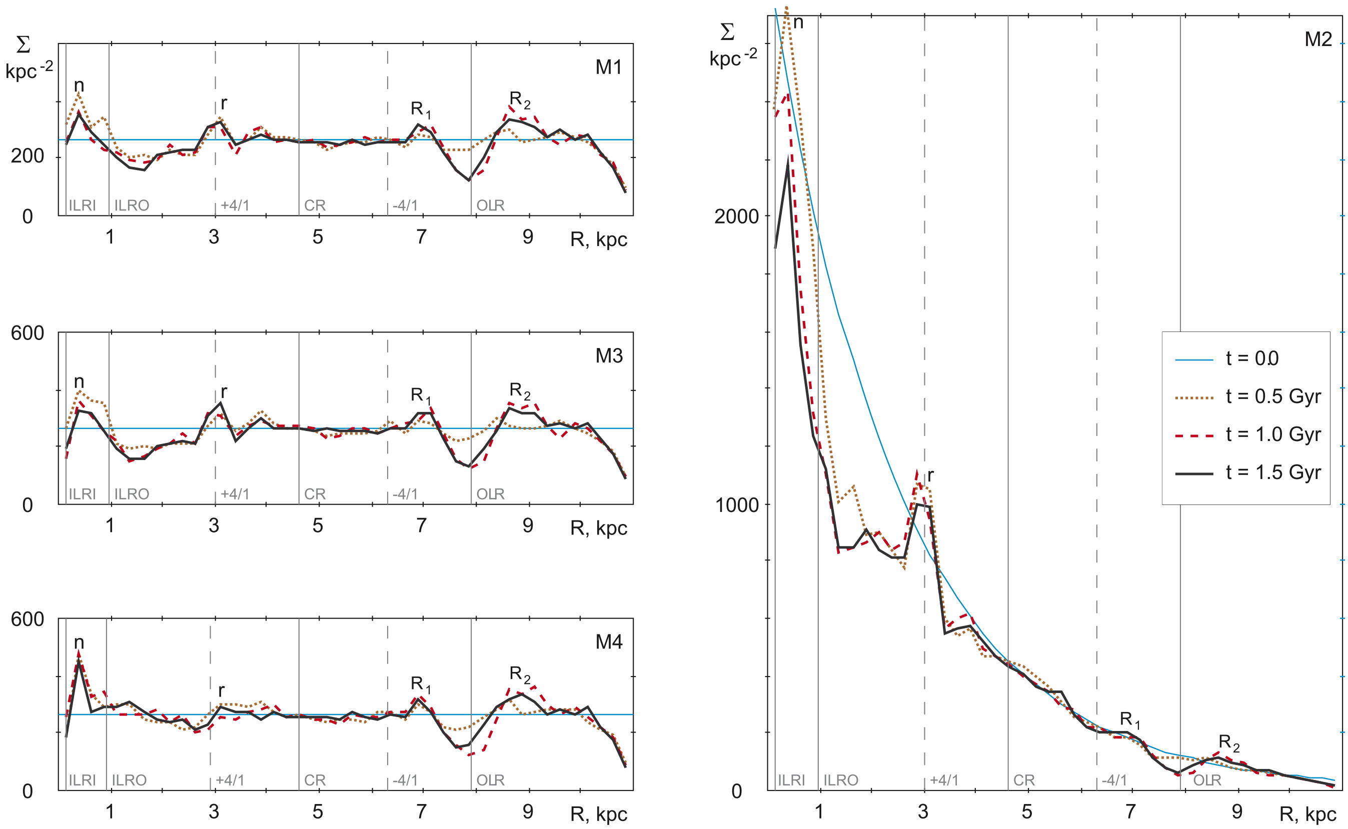

Figure 11. Profiles of the surface density Σ built for the distribution of model particles (gas + OB) in models 1–4 at several time moments: $t = 0.0$, 0.5, 1.0 and 1.5 Gyr. Density maxima related to the resonance rings are designated by letters: n – nuclear rings, r – inner rings, R_1 and R_2 – outer rings. The locations of the resonances are also indicated. The profile built for model 2 exhibits a larger range of density variations, but the scale is the same in all frames. We can see that the nuclear rings achieve maximum density at the time moment $t = 0.5$ Gyr, while the outer rings have maximum Σ in the interval $t = 1.0$–1.5 Gyr. The surface density excesses above the background are nearly the same in the two outer rings, but the rings R_2 are nearly twice as wide as R_1 in all models. This suggests that the rings R_2 manage to catch twice as many particles as R_1.

choice of $\theta_{\rm b}$ and agree with the observed velocities for any $\theta_{\rm b}$ from the interval considered.

Thus the model and observed velocities, $V_{\rm R}$ and $V_{\rm T}$, in the three star-gas complexes (Sagittarius, LS and Perseus) agree within the errors for position angle $\theta_{\rm b}$ lying in the interval 40–52°.

4.3 Surface-density profiles

The formation of resonance rings can be traced by the surface-density profiles. Fig. 11 shows the variations of the surface density Σ of model particles (gas + OB) with galactocentric distance R for models 1–4 at four time moments: $t = 0.0$, 0.5, 1.0 and 1.5 Gyr. These profiles clearly indicate the positions of the resonance rings.

The nuclear rings (n) form between the two ILRs at a distance of $R = 0.2$–0.9 kpc (Fig. 11). The surface density of the nuclear rings achieves a maximum at the time moment $t \sim 0.5$ Gyr and then starts decreasing. This process is fastest in model 2, which could be due to the largest frequency of collisions occurring there.

The inner rings (r) are growing for distance $R = 3.0$–3.3 kpc, which is slightly larger than that of the 4/1 resonance. Note that an inner ring is practically absent in model 4 – we can see only a small density enhancement at $t = 0.5$ Gyr there. Interestingly, the conspicuous diamond-shape structures inside the Ferrers ellipsoid visible in many frames of Fig. 4 at distances 1–3 kpc appears to lie in the region with reduced surface density (Fig. 11).

The outer rings, R_1 and R_2, emerge at distances 6.7–7.3 and 8.5–9.3 kpc, respectively (Fig. 11). They achieve maximum Σ in the interval $t = 1.0$–1.5 Gyr, though the rings R_2 grow more slowly. The surface density enhancements above the background are nearly the same in the two outer rings. However, the rings R_2 are nearly twice as wide as R_1 in all models, which suggests that rings R_2 manage to catch twice as many particles as rings R_1.

On the whole, the positions and growth rate of the resonance rings in the models considered agree with the estimates obtained in previous simulations (Schwarz 1981; Byrd et al. 1994; Buta & Combes 1996; Rautiainen & Salo 1999, 2000; Melnik & Rautiainen 2009; Rautiainen & Melnik 2010).

4.4 Velocity dispersion

The velocity perturbations from the bar give rise to both systematic motions and velocity dispersions. To separate the random and systematic velocities, we divide model discs into annuli of 0.5 kpc width and then partition every annulus into cells of ∼0.5 kpc length in the azimuthal direction. Different annuli contain different numbers of cells. The velocities of model particles inside every cell are assumed to obey a linear law:

$$V_{\rm R} = V_1 + A_1(R - R_{\rm c}) + B_1(\theta - \theta_{\rm c}) + \xi, \tag{12}$$

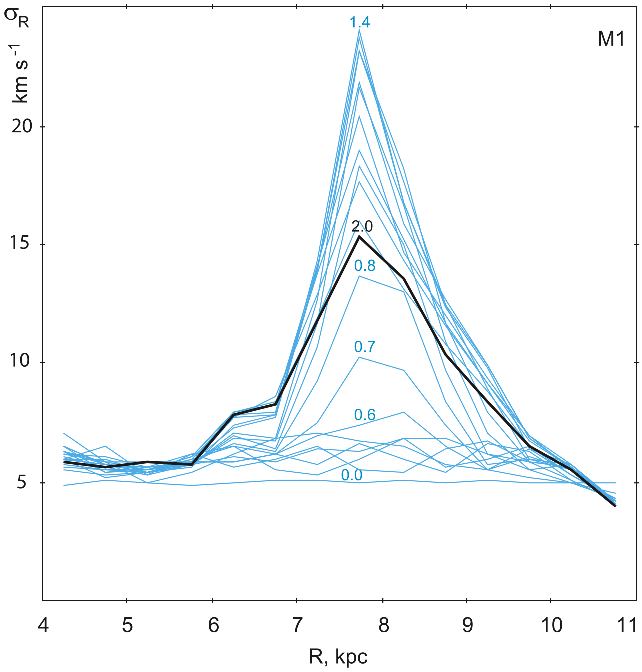

Figure 12. Dependence of velocity dispersion $\sigma_{\rm R}$ on galactocentric radius R in model 1 at time moments t from $t = 0$–2.0 Gyr with a time interval of 0.1 Gyr. The profile related to $t = 2.0$ Gyr is distinguished by the thick black line, while other profiles are depicted by the thin grey lines (coloured blue in the online article). Numbers near some profiles indicate the time moments in Gyr. The velocity dispersion $\sigma_{\rm R}$ achieves a maximum at a radius of ∼8 kpc at time moment $t = 1.4$ Gyr, but then it starts decreasing. All values of $\sigma_{\rm R}$ located above the value of 15 km s^{-1} can be considered as overestimated, due to the contribution of systematic radial velocities.

$$V_{\rm T} = V_2 + A_2(R - R_{\rm c}) + B_2(\theta - \theta_{\rm c}) + \eta, \quad (13)$$

where $R_{\rm c}$ and $\theta_{\rm c}$ are the galactocentric radius and galactocentric angle of the centre of a cell; V_1 and V_2 are the average velocities of model particles (gas + OB) in the cell in the radial and azimuthal directions, respectively; the parameters A_1, B_1, A_2 and B_2 describe changes of systematic velocities in the radial and azimuthal directions, while values ξ and η characterize random deviations from the linear law. In the first approximation, the standard deviations of values ξ and η in every cell represent the velocity dispersions in the radial and azimuthal directions, $\sigma_{\rm R}$ and $\sigma_{\rm T}$, respectively. The average values of $\sigma_{\rm R}$ and $\sigma_{\rm T}$ calculated for all cells located in the same annulus give us a smooth distribution of the velocity dispersion with galactocentric radius.

Fig. 12 shows the changes in velocity dispersion $\sigma_{\rm R}$ with galactocentric distance R in model 1 at different time moments. We can see the fast growth of $\sigma_{\rm R}$ in the time interval 0.5–1.4 Gyr, with a maximal value of 23 km s^{-1} being achieved at a radius of ∼8 kpc, but then $\sigma_{\rm R}$ declines by 15 km s^{-1}. All models demonstrate a similar growth and decline in $\sigma_{\rm R}$. Probably, it is the process of formation of the outer rings that is responsible for the extra increase in velocity dispersion $\sigma_{\rm R}$ in the time interval 1.0–1.4 Gyr. We merely cannot separate systematic and random motions properly during this process. The drop in $\sigma_{\rm R}$ by the end of the simulation is due to decreasing systematic motions, which decline especially quickly in ring R_2 (see variations of $V_{\rm R}$ in the Perseus region: Fig. 6, Table 5). Generally, the value of 15 km s^{-1} can be considered as the upper estimate of $\sigma_{\rm R}$ at the radius of the OLR.

Note that Fig. 12 exhibits velocity dispersion in the interval of galactocentric distances from 4–11 kpc only. In the central region, the velocity dispersion achieves considerably higher values. For example, at the distance of the nuclear ring, $R \approx 0.5$ kpc, $\sigma_{\rm R}$ reaches ∼100 km s^{-1}.

The velocity dispersion $\sigma_{\rm T}$ grows during the time interval 0.5–1.4 Gyr and reaches 10 km s^{-1}, which is nearly twice as small as the maximum of $\sigma_{\rm R}$, but then $\sigma_{\rm T}$ decreases by a value of 7 km s^{-1}.

Fig. 13(a) shows the radial oscillations of two model particles which appear to lie inside the Local System in model 3 (one without collisions) at time moment $t = 1.5$ Gyr. The chosen particles represent oscillations occurring in opposite phases. The growth of the amplitudes is evidence of resonance. Fig. 13(b) demonstrates variations of specific angular momentum L and will be discussed in Section 4.5. Figs 13(c) and 13(d) represent the orbits of these particles in a reference frame corotating with the bar. We can see that particle 1 supports the outer ring R_1 while particle 2 supports ring R_2. Note that particle 1 has positive radial velocity $V_{\rm R}$ at $t = 1.5$ Gyr, when it lies inside the Local System, while particle 2 has negative velocity $V_{\rm R}$ at the same moment.

Fig. 13(a) indicates that particle 1 has a maximal amplitude of radial oscillations at $t = 0.9$ Gyr approaching distances of 6.9 and 8.4 kpc, but then the oscillations start fading. Particle 2 deviates considerably from its initial radius, $R = 7.5$ kpc, approaching distances of 10.0 and 6.8 kpc. Moreover, the deviations of particle 2 in the direction away from the galactic centre are larger than those in the opposite direction, suggesting an increase of its average distance R.

Fig. 13(d) shows that the orbit of particle 2 is not at first aligned with the bar, being stretched at an angle of ∼45° with respect to the bar major axis and taking an intermediate position between the orientations of orbits in rings R_1 and R_2. However, the orbit has achieved the right orientation, being elongated along the bar, by time $t = 1.5$ Gyr. This adjustment of orbits causes changes in both systematic velocities and velocity dispersions.

There is a question as to whether such large values of velocity dispersion $\sigma_{\rm R}$ emerging near the OLR agree with observations. The velocity dispersion $\sigma_{\rm R}$ achieves large values, $\sigma_{\rm R} \approx 15$ km s^{-1}, in the small interval of Galactocentric distances 7.5–8.5 kpc. However, this interval corresponds to a minimum in the distribution of the surface density of model particles (Fig. 11). Probably, the number of particles with large velocity dispersion is not high. To check this, we have selected OB particles located within 3 kpc of the adopted solar position ($R_0 = 7.5$ kpc, $\theta_{\rm b} = 45°$) and derived the parameters of the rotation curve and velocity dispersion from model velocities. Here, we supposed that model particles move in circular orbits, in accordance with Galactic differential rotation. The same method was applied to observational data (Melnik & Dambis 2009). The derived rotation curve appears to be in good agreement with the observed rotation curve. The standard deviation σ_v of the velocities of OB particles from the rotation curve computed jointly for radial and azimuthal directions proves to be 11 km s^{-1} (model 1, $t = 1.5$ Gyr). It is slightly larger than the σ_v obtained for observed OB associations (7–8 km s^{-1}, Melnik & Dambis 2017), but still smaller than the σ_v calculated for young open clusters (15 km s^{-1}, Melnik et al. 2016) and close to the σ_v derived for classical Cepheids (10–11 km s^{-1}, Melnik et al. 2015). The fraction of particles with $|V_{\rm R}| > 15$ km s^{-1} appears to be only 7 per cent, but their exclusion decreases the velocity dispersion to a value of $\sigma_v = 6$ km s^{-1}.

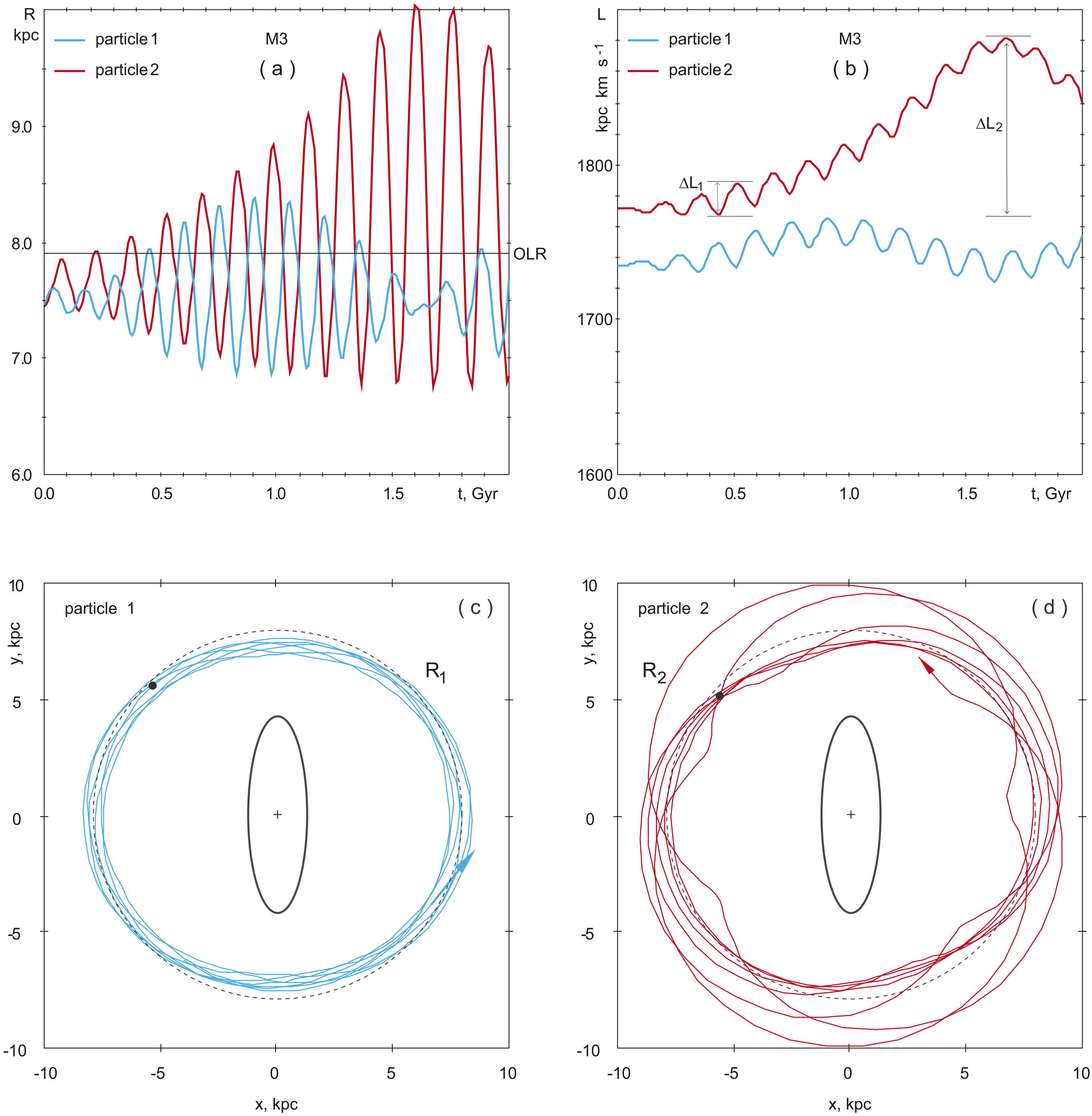

Figure 13. (a) Radial oscillations of two model particles (model 3) which appear to lie inside the Local System at the time moment $t = 1.5$ Gyr. The oscillations of particle 1 (coloured blue in the online article) and particle 2 (coloured red in the online article) support outer rings R_1 and R_2, respectively. (b) Variations of specific angular momentum L of two chosen particles. (c) Orbit of particle 1 in a reference frame corotating with the bar. The ellipse indicates the position of the bar. The thin dashed line shows the radius of the OLR. A black circle in the upper left corner highlights the position of the particle at $t = 1.5$ Gyr. (d) Orbit of particle 2 in a reference frame corotating with the bar (see details above).

4.5 Distribution of angular momentum

The rotation of the bar in a galactic disc causes the redistribution of the specific angular momentum L:

$$L = \Theta R \tag{14}$$

along the galactocentric distance R, where Θ is the velocity in the azimuthal direction.

So far, we have considered the kinematics near the OLR of the bar only, but in this section it makes sense to study motions near both Lindblad resonances: ILR and OLR. The redistribution of angular momentum L near both Lindblad resonances seems to have one physical reason.

Fig. 14(a) shows the distribution of the azimuthal velocities Θ of model particles (gas + OB) averaged in thin annuli of 40 pc width along the galactocentric distance R in model 1 at $t = 1.5$ Gyr.

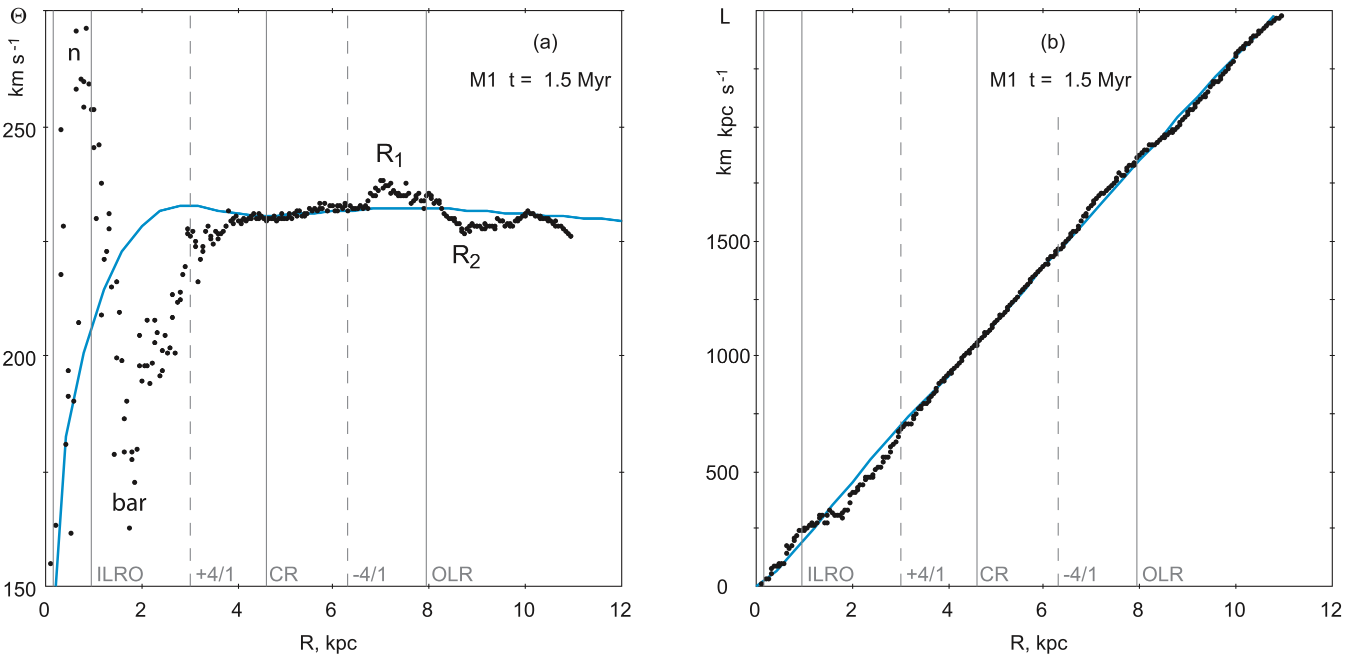

Figure 14. (a) Distribution of the azimuthal velocity Θ (black circles) of model particles (gas + OB) averaged in thin annuli of 40 pc width with galactocentric radius R in model 1 at $t = 1.5$ Gyr. The grey line (coloured blue in the online article) shows the velocity of the rotation curve, V_c, which reflects the initial distribution of Θ. The vertical grey lines indicate the positions of the resonances. We can see that the average azimuthal velocity Θ, and consequently L, increases in the nuclear region (n) and in the R_1 region, while Θ and L decrease in the bar region and in the R_2 region. (b) Distribution of the specific angular momentum L (circles) of model particles averaged in thin annuli of 40 pc width along the distance R. The grey line (coloured blue in the online article) indicates the initial distribution of L. The most significant changes of L occur in the bar region.

Also shown is the velocity of the rotation curve, V_c, which reflects the initial distribution of Θ. We can see that particles located near the ILR and OLR of the bar change their velocity Θ in a similar way, forming a hump and a pit near the radius of the resonance. The average azimuthal velocity Θ, and consequently L, increases (decreases) at radii slightly smaller (larger) than those of the Lindblad resonances. In the neighbourhood of the ILR, the velocity Θ grows at the distance of the nuclear ring and decreases in the region of the most populated bar orbits. In the vicinity of the OLR, the velocity Θ increases and decreases at the distances of rings R_1 and R_2, respectively. Fig. 14(b) demonstrates the distribution of the specific angular momentum L of model particles averaged in thin annuli. The initial distribution of L is also indicated. It is seen that the most significant changes of L occur in the bar region. Note that all models demonstrate similar behaviour.

As the bar creates accelerations in the azimuthal direction, angular momentum L is not conserved in barred galaxies. However, most particles on their quasi-periodic orbits acquire and lose nearly the same value of angular momentum, ΔL, during their revolution with respect to the bar.

Fig. 13(b) presents the oscillations of specific angular momentum of the two particles supporting the outer rings R_1 and R_2. We can see fast oscillations of the angular momentum, ΔL_1, with a period of ∼150 Myr, corresponding to half their revolution period with respect to the bar. The range (twice amplitude) of these changes is $\Delta L_1 \approx 20$ km kpc s^{-1}. Besides the fast oscillations, we can see slower ones. For example, particle 2 increases its angular momentum by a value $\Delta L_2 \approx 100$ km kpc s^{-1} during the formation of ring R_2 in the time interval 1–1.5 Gyr. However, both these values correspond to quite small changes of R. Fig. 14(b) demonstrates nearly linear growth of angular momentum L with increasing R. Using equation (14) and the value of $\Theta = 232$ km s^{-1}, we can estimate the variations in R corresponding to ΔL_1 and ΔL_2, which appear to be $\Delta R_1 = 0.1$ and $\Delta R_2 = 0.4$ kpc, respectively. Both these values are small in comparison with the range (twice the amplitude) of radial oscillations of particle 1 and 2, equal to $\Delta R = 1.5$ and 3.2 kpc, respectively (Fig. 13a). Thus, model particles show only small variations of L during their radial oscillations.

Resonance amplifies epicyclic motions and throws particles to distances corresponding to larger changes of their angular momenta than ΔL_1 and ΔL_2 received from the bar. Particles from smaller distances R having smaller angular momenta L can move to larger distances, at which particles initially have larger L, and vice versa. The average values of the azimuthal velocity Θ and L therefore decrease (increase) at radii slightly larger (smaller) than those of the Lindblad resonances.

Probably, the redistribution of L near the Lindblad resonances of the bar is due to the existence of elongated periodic orbits, which catch many particles from nearby space. The residual azimuthal velocities V_T are directed in opposite senses at the apocentres (outermost points) and pericentres (innermost points) of periodic orbits.

Fig. 15 shows the directions of the residual velocities at different points of periodic orbits supporting the nuclear ring, bar and outer rings. The additional (residual) azimuthal velocity V_T is directed in a sense opposite to that of the galactic rotation ($V_T < 0$) at the apocentres (A, A', F, F', C and C') of elongated periodic orbits, while V_T is directed in the sense of the galactic rotation ($V_T > 0$) at the pericentres (E, E', B, B', D and D'). The radial velocity V_R attains extreme values at points lying at angles of about ±45° with respect to the bar axes.

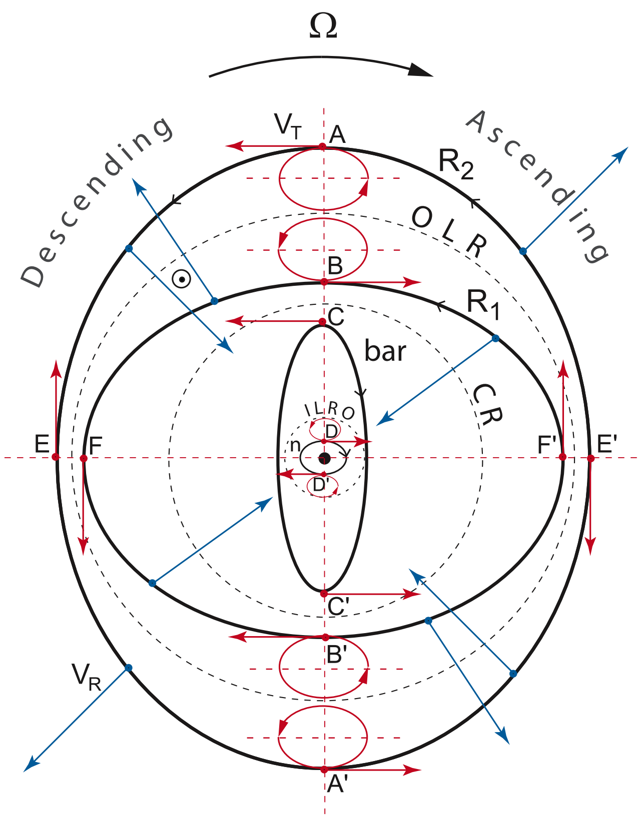

Figure 15. Schematic description of epicyclic motions at different points of periodic orbits supporting the nuclear ring (n), bar, outer ring R_1 and R_2. The additional velocity $V_{\rm T}$ due to epicyclic motions (coloured red in the online article) is directed in a sense opposite to that of the galactic rotation at the apocentres (A, $A^{'}$, F, $F^{'}$, C and $C^{'}$) of periodic orbits and in the sense of the galactic rotation at the pericentres (E, $E^{'}$, B, $B^{'}$, D and $D^{'}$). The radial velocity $V_{\rm R}$ (coloured blue in the online article) attains extreme values at points lying at about ±45° with respect to the bar axes. The galaxy rotates clockwise, but, in the reference frame corotating with the bar, objects located outside the CR, including those related to the outer rings, are moving counterclockwise. The Sun is supposed to lie at $\theta_{\rm b} = 45°$ with respect to the bar major axis near the descending segment ($V_{\rm R} < 0$) of the ring R_2.

Probably, the tuning of epicyclic motions (Fig. 15) causes the appearance of annuli with deficiency and excess of angular momentum L. These annuli must be located some distance away from the Lindblad resonances, because, at precisely the radii of the resonances, there are both pericentres and apocentres of periodic orbits oriented perpendicular to each other. For example, we can see that the apocentres (F and $F^{'}$) and pericentres (E and $E^{'}$) of periodic orbits existing near the OLR are located at practically the radius of the OLR, so the average value of the azimuthal velocity Θ must be close to that of the rotation curve there. However, at some distance away from the Lindblad resonances there is nothing to compensate for the systematic changes in azimuthal velocity. The deficiency of L ($V_{\rm T} < 0$) corresponds to the apocentres (A, $A^{'}$, C and $C^{'}$) of periodic orbits oriented along the bar, while the excess of L ($V_{\rm T} > 0$) occurs at the pericentres (B, $B^{'}$, D and $D^{'}$) of periodic orbits elongated perpendicular to the bar. Thus, the redistribution of L along the radius is caused by the existence of two types of stable periodic orbit elongated perpendicular to each other near the Lindblad resonances of the bar.

Let us imagine the motions of two particles located near points E and F at some moment and call them, for simplicity, particles E and F, respectively (Fig. 15). Due to galactic differential rotation, particle E, which lies at a slightly larger R, must rotate with a slightly smaller angular velocity Ω than particle F, so particle E must drift counterclockwise in the azimuthal direction with respect to particle F. However, the epicyclic motions adjusted by the resonance can slow down or even change the direction of this drift. The velocity $V_{\rm T}$ at point E is directed in such a way as to increase Ω, while $V_{\rm T}$ at point F must decrease Ω. Thus, the resonance can cause the rotation of particles E and F with the same angular velocity for some time period. This co-rotation does not affect the velocities of massless test particles in models without self-gravity, such as in the case considered. However, if self-gravity is included, then this co-motion can create favorite conditions for the growth of overdensities (Julian & Toomre 1966; Toomre 1981; Sellwood & Kahn 1991) and the formation of slow modes (Rautiainen & Salo 2000; Rautiainen & Melnik 2010; Melnik & Rautiainen 2013).

5 CONCLUSIONS

We studied models with analytical Ferrers bars and compared the velocities of model particles with the observed velocities of OB associations. Two power indexes in the density distribution inside the Ferrers ellipsoids were considered: $n = 2$ (models 1–3) and $n = 1$ (model 4). The initial surface-density distribution of model particles is exponential in model 2 and uniform in other models. Model 3 does not include collisions, but in other models particles can collide with each other inelastically.

All models considered can reproduce the observed residual velocities (those after subtraction of the velocities due to the rotation curve and solar motion towards the apex) of OB associations in the Sagittarius, Local System and Perseus star-gas complexes. There are many moments during the time interval 1–2 Gyr after the start of simulations when model and observed velocities agree within the errors (Fig. 6).

The success in reproduction of velocities in the Local System is due to the large velocity dispersion of the model particles, which weakens resonance effects by producing smaller systematic velocity changes.

The model and observed residual velocities in the Sagittarius, Local System and Perseus star-gas complexes agree within the errors for solar position angle $\theta_{\rm b} = 40$–$52°$ (Fig. 10).

The angular velocity of the bar is chosen to be $\Omega_{\rm b} = 50$ km s^{-1} kpc^{-1}, which corresponds to the location of the OLR of the bar 0.4 kpc outside the solar circle, $R_{\rm OLR} = R_0 + 0.4$ kpc. The uncertainty in determination of $\Omega_{\rm b}$ is less than ±2 km s^{-1} kpc^{-1}.

Model galaxies form nuclear, inner and outer resonance rings. Nuclear rings appear between the two ILRs at a distance ∼0.5 kpc from the centre. The inner rings grow at a radius of ∼3.3 kpc, which is slightly larger than that of the 4/1 resonance. The outer rings, R_1 and R_2, form at radii of ∼7.0 and ∼8.8 kpc, respectively. The surface density excess is nearly the same in the two outer rings. However, the rings R_2 are nearly twice as wide as R_1 in all models, which means that the rings R_2 manage to catch twice as many particles as R_1 (Fig. 11).

The dispersion of radial velocities, $\sigma_{\rm R}$, never drops below 5 km s^{-1} in the models considered. It shows conspicuous growth at the radius of the OLR, attaining a maximal value of 23 km s^{-1} at 1.4 Gyr, but then declines by 15 km s^{-1}. The extra growth in velocity dispersion near the OLR seems to be connected with a difficulty in separation between systematic and random motions during the formation of the outer ring R_2 (Fig. 12).

Model particles demonstrate the redistribution of specific angular momentum L near the ILR and OLR of the bar (Fig. 14). The average value of the azimuthal velocity Θ and consequently L increases (decreases) at radii slightly smaller (larger) than those of the Lindblad resonances. The most significant changes of L occur in the bar region. Probably, the redistribution of L with radius is caused by the existence of two types of stable periodic orbit elongated perpendicular to each other near the Lindblad resonances of the bar (Fig. 15).

ACKNOWLEDGEMENTS

I thank the anonymous referee for fruitful discussion. I thank P. Rautiainen and A. K. Dambis for useful remarks and suggestions. This work has made use of data from the European Space Agency (ESA) mission *Gaia* (https://www.cosmos.esa.int/gaia), processed by the *Gaia* Data Processing and Analysis Consortium (DPAC, https://www.cosmos.esa.int/web/gaia/dpac/consortium). Funding for the DPAC has been provided by national institutions, in particular the institutions participating in the *Gaia* Multilateral Agreement.

REFERENCES

Antoja T. et al., 2018, Nature, 561, 360
Athanassoula E., 1984, Phys. Rep., 114, 321
Athanassoula E., 1992, MNRAS, 259, 328
Athanassoula E., 2005, MNRAS, 358, 1477
Athanassoula E., Sellwood J. A., 1986, MNRAS, 221, 213
Athanassoula E., Bienayme O., Martinet L., Pfenniger D., 1983, A&A, 127, 349
Athanassoula E., Romero-Gómez M., Masdemont J. J., 2009, MNRAS, 394, 67
Baba J., Asaki Y., Makino J., Miyoshi M., Saitoh T. R., Wada K., 2009, ApJ, 706, 471
Baba J., Saitoh T. R., Wada K., 2013, ApJ, 763, 46
Benjamin R. A. et al., 2005, ApJ, 630, L149
Bertin G., Lin C. C., 1996, Spiral Structure in Galaxies: A Density Wave Theory. MIT Press, Cambridge, MA
Binney J., Tremaine S., 1987, Galactic Dynamics. Princeton Univ. Press, Princeton, New Jersey
Blaha C., Humphreys R. M., 1989, AJ, 98, 1598
Block D. L., Puerari I., Knapen J. H., Elmegreen B. G., Buta R., Stedman S., Elmegreen D. M., 2001, A&A, 375, 761
Bobylev V. V., Bajkova A. T., 2018, Astron. Lett., 44, 676
Boehle A. et al., 2016, ApJ, 830, 17
Brahic A., Henon M., 1977, A&A, 59, 1
Branham R. L., 2017, Ap&SS, 362, 29
Bressan A., Marigo P., Girardi L., Salasnich B., Dal Cero C., Rubele S., Nanni A., 2012, MNRAS, 427, 127
Brown A. G. A. et al., 2018, A&A, 616, A1
Buta R., 1995, ApJS, 96, 39
Buta R., 2017, MNRAS, 471, 4027
Buta R., Combes F., 1996, Fund. Cosmic Phys., 17, 95
Buta R., Crocker D. A., 1991, AJ, 102, 1715
Buta R., Laurikainen E., Salo H., 2004, AJ, 127, 279
Byrd G., Rautiainen P., Salo H., Buta R., Crocker D. A., 1994, AJ, 108, 476
Cabrera-Lavers A., Hammersley P. L., González-Fernández C., López-Corredoira M., Garzón F., Mahoney T. J., 2007, A&A, 465, 825
Churchwell E. et al., 2009, PASP, 121, 213
Combes F., Sanders R. H., 1981, A&A, 96, 164
Comerón S. et al., 2014, A&A, 562, 121
Contopoulos G., Grosbol P., 1989, A&AR, 1, 261
Contopoulos G., Papayannopoulos Th., 1980, A&A, 92, 33
D'Onghia E., Vogelsberger M., Hernquist L., 2013, ApJ, 766, 34
Dambis A. K., Berdnikov L. N., Kniazev A. Y., Kravtsov V. V., Rastorguev A. S., Sefako R., Vozyakova O. V., 2013, MNRAS, 435, 3206
de Vaucouleurs G., Freeman K. C., 1972, Vistas Astron., 14, 163
Debattista V. P., Sellwood J. A., 2000, ApJ, 543, 704
Dehnen W., Binney J., 1998, MNRAS, 294, 429
Díaz-García S., Salo H., Laurikainen E., Herrera-Endoqui M., 2016, A&A, 587, 160
Dwek E. et al., 1995, ApJ, 445, 716
Efremov Yu. N., Sitnik T. G., 1988, Sov. Astron. Lett., 14, 347
Elmegreen B. G., Elmegreen D. M., 1985, ApJ, 288, 438
Elmegreen D. M., Elmegreen B. G., Bellin A. D., 1990, ApJ, 364, 415
Feast M. W., Laney C. D., Kinman T. D., van Leeuwen F., Whitelock P. A., 2008, MNRAS, 386, 2115
Ferrers N. M., 1877, Q. Appl. Math., 14, 1
Francis Ch., Anderson E., 2014, MNRAS, 441, 1105
Freeman K. C., 1970, ApJ, 160, 811
Fujii M. S., Bédorf J., Baba J., Portegies Zwart S., 2018, MNRAS, 477, 1451
Fujii M. S., Bédorf J., Baba J., Portegies Zwart S., 2019, MNRAS, 482, 1983
Georgelin Y. M., Georgelin Y. P., 1976, A&A, 49, 57
Gerhard O., 2011, Mem. Soc. Astron. Ital. Suppl., 18, 185
Glushkova E. V., Dambis A. K., Melnik A. M., Rastorguev A. S., 1998, A&A, 329, 514
González-Fernández C., López-Corredoira M., Amôres E. B., Minniti D., Lucas P., Toledo I., 2012, A&A, 546, 107
Grand R. J., Kawata D., Cropper M., 2012, MNRAS, 421, 1529
Groenewegen M. A. T., Udalski A., Bono G., 2008, A&A, 481, 441
Grosbøl P., Carraro G., 2018, A&A, 619, 50
Julian W. H., Toomre A., 1966, ApJ, 146, 810
Jung Ch., Zotos E. E., 2016, MNRAS, 463, 3965
Kalnajs A. J., 1991, in Sundelius B., ed., Dynamics of Disc Galaxies. Göteborgs Univ., Göthenburg, p. 323
Katz D. et al., 2018, A&A, 616, A11
Kawata D., Baba J., Ciuca I., Cropper M., Grand R. J. J., Hunt J. A. S., Seabroke G., 2018, MNRAS, 479, 108
Kormendy J., Kennicutt R. C., 2004, ARA&A, 42, 603
Laurikainen E., Salo H., Buta R., 2005, MNRAS, 362, 1319
Levinson F. H., Roberts W. W., 1981, ApJ, 245, 465
Li Z., Shen J., 2012, ApJ, 757, L7
Li Z., Shen J., Kim W.-T., 2015, ApJ, 806, 150
Lindegren L. et al., 2018, A&A, 616, A2
Lin C. C., Shu F. H., 1964, ApJ, 140, 646
Mark J. W.-K., 1976, ApJ, 205, 363
Martinez-Valpuesta I., Aguerri J. A. L., González-García A. C., Dalla V. C., Stringer M., 2017, MNRAS, 464, 1502
Melnik A. M., Dambis A. K., 2009, MNRAS, 400, 518
Melnik A. M., Dambis A. K., 2017, MNRAS, 472, 3887
Melnik A. M., Rautiainen P., 2009, Astron. Lett., 35, 609
Melnik A. M., Rautiainen P., 2011, MNRAS, 418, 2508
Melnik A. M., Rautiainen P., 2013, MNRAS, 434, 1362
Melnik A. M., Rautiainen P., Berdnikov L. N., Dambis A. K., Rastorguev A. S., 2015, Astron. Nachr., 336, 70
Melnik A. M., Rautiainen P., Glushkova E. V., Dambis A. K., 2016, Ap&SS, 361, 60
Melvin T., Masters K., the Galaxy Zoo Team, 2013, Mem. Soc. Astron. Ital. Suppl., 25, 82
Méndez-Abreu J., Sánchez-Janssen R., Aguerri J. A. L., Corsini E. M., Zarattini S., 2012, ApJ, 761, L6
Michikoshi S., Kokubo E., 2014, ApJ, 787, 174
Nataf D. M., 2017, PASA, 34, 41
Ness M., Lang D., 2016, AJ, 152, 14
Nikiforov I. I., 2004, in Byrd G. G., Kholshevnikov K. V., Myllri A. A., Nikiforov I. I., Orlov V. V., eds, ASP Conf. Ser. Vol. 316, Order and Chaos in Stellar and Planetary Systems. Astron. Soc. Pac., San Francisco, p. 199
Ostriker J. P., Peebles P. J. E., 1973, ApJ, 186, 467

Pettitt A. R., Dobbs C. L., Acreman D. M., Price D. J., 2014, MNRAS, 444, 919
Pettitt A. R., Dobbs C. L., Acreman D. M., Bate M. R., 2015, MNRAS, 449, 3911
Pfenniger D., 1984, A&A, 134, 373
Pohl M., Englmaier P., Bissantz N., 2008, ApJ, 677, 283
Ramos P., Antoja T., Figueras F., 2018, A&A, 619, 72
Rastorguev A. S., Utkin N. D., Zabolotskikh M. V., Dambis A. K., Bajkova A. T., Bobylev V. V., 2017, Astrophys. Bull., 72, 122
Rautiainen P., Melnik A. M., 2010, A&A, 519, 70
Rautiainen P., Salo H., 1999, A&A, 348, 737
Rautiainen P., Salo H., 2000, A&A, 362, 465
Rautiainen P., Salo H., Laurikainen E., 2008, MNRAS, 388, 1803
Reid M. J., Menten K. M., Zheng X. W., Brunthaler A., Xu Y., 2009, ApJ, 705, 1548
Roberts W. W., Hausman M. A., 1984, ApJ, 277, 744
Rodriguez-Fernandez N. J., Combes F., 2008, A&A, 489, 115
Romero-Gómez M., Athanassoula E., Masdemont J. J., García-Gómez C., 2007, A&A, 472, 63
Russeil D., 2003, A&A, 397, 133
Salo H., 1991, A&A, 243, 118
Sanders R. H., Tubbs A. D., 1980, ApJ, 235, 803
Schwarz M. P., 1981, ApJ, 247, 77
Sellwood J. A., Wilkinson A., 1993, Rep. Prog. Phys., 56, 173
Sellwood J. A., Kahn F. D., 1991, MNRAS, 250, 278
Shen J., Rich R. M., Kormendy J., Howard C. D., De Propris R., Kunder A., 2010, ApJ, 720, L72
Sheth K. et al., 2008, ApJ, 675, 1141
Sheth K. et al., 2010, PASP, 122, 1397
Simion I. T., Belokurov V., Irwin M., Koposov S. E., Gonzalez-Fernandez C., Robin A. C., Shen J., Li Z.-Y., 2017, MNRAS, 471, 4323
Sormani M. C., Sobacchi E., Fragkoudi F., Ridley M., Treß R. G., Glover S. C. O., Klessen R. S., 2018, MNRAS, 481, 2
Toomre A., 1969, ApJ, 158, 899
Toomre A., 1977, ARA&A, 15, 437
Toomre A., 1981, in Fall S. M., Lynden-Bell D., eds, The Structure and Evolution of Normal Galaxies. Cambridge Univ. Press, Cambridge, p. 111
Vallée J. P., 2015, MNRAS, 450, 4277
Xu Y. et al., 2018, A&A, 616, L15

This paper has been typeset from a TEX/LATEX file prepared by the author.